Journal of Manufacturing Processes 172 (2026) 490–511

Contents lists available at ScienceDirect

Journal of Manufacturing Processes

journal homepage: www.elsevier.com/locate/manpro

# Centerless grinding as an affine profile transformation: Physics-based and data-driven approaches

Lohit Kumar Pentakota [a,b], Marco Leonesio [a], Moschos Papananias [c,*], Giacomo Bianchi [a]

[a] CNR – STIIMA, Institute of Intelligent Industrial Technologies and Systems for Advanced Manufacturing National Research Council of Italy, Via Alfonso Corti 12, 20133, Milan, Italy

[b] Department of Informatics, Bioengineering, Robotics and Systems Engineering, University of Genova, Via alla Opera Pia, 13, 16145, Genova, Italy

[c] Department of Mechanical and Aerospace Engineering, Brunel University of London, Kingston Lane, Uxbridge, Middlesex, UB8 3PH, UK

ARTICLE INFO

*Keywords:*
Centreless grinding
Process modelling
Affine transformation
Data-driven identification

ABSTRACT

Material removal processes are industrially adopted to transform a given initial workpiece geometry into a final one with desired properties in terms of shape and accuracy. This paper analyses the modelling of the centerless grinding process as a direct mathematical transformation between the initial and final workpiece profiles. By modelling the grinding process as a discrete linear dynamical system, each stage of the operation (e.g., roughing and finishing) can be described as an affine transformation operated by a constant transition matrix that embeds the linearized discrete process dynamics, and an offset component that reproduces the nominal material removal due to axis feed. Relying on an opportune state augmentation, the affine transformation includes a linear-phase low pass filter that reproduces the contact filtering effect due to wheel and workpiece engagement. The affine transformation can be built starting from the static physics-based model of the process but also identified from grinding experiments, following a purely data-driven approach, by solving an over-determined linear system on the measured initial and final profiles. For this latter case, the identification accuracy is analysed relying on "virtual experiments" provided by a high-fidelity non-linear process model that allows the effect of all involved phenomena, like structural dynamics and grinding wheel-workpiece detachment, to be investigated. The proposed affine model, in addition to allowing a rapid estimation of the final profile quality, provides interesting insight into the properties of the process in terms of profile transformation.

## 1. Introduction

The centerless grinding process is extensively used in industry due to its efficient system for loading and unloading workpieces (WPs). In this process, the WP is placed between the grinding (operating) wheel and the control (rubbing or regulating) wheel, while being supported by a work rest blade (see Fig. 1). This setup eliminates the need for clamping devices and centering procedures, leading to significant time savings and higher productivity compared to other centered grinding methods [1]. Unfortunately, the absence of a centering device can lead to unstable operations if the setup parameters are not carefully chosen. This instability can be attributed to two different phenomena that may interact: regenerative chatter and geometric lobing [2].

Regenerative chatter is a common issue in all machining processes and is caused by the interaction between the cutting process and the machine's structural dynamics [3]. In centerless grinding, it interacts with geometric instability, also known as the "lobing effect", which is intimately related to geometrical parameters like blade angle and WP height. In fact, any initial deviation in the WP profile interacts with both the control wheel and the supporting blade during rotation, causing unwanted oscillations of the WP center. These oscillations lead to irregular material removal, which can exacerbate WP imperfections. This so-called "rounding mechanism," as studied by Furukawa et al. in [4], is crucial for achieving smooth WP profiles but can also be a source of instability [5,6]. Furthermore, continuous improvement in component roundness accuracy through Computer Numerical Control (CNC) centreless grinding, particularly in high-productivity environments, is becoming more and more challenging, especially in modern automotive and bearing manufacturing. For example, grinding engine valve rods, now, targets a roundness accuracy of down to 0.1 μm due to increasingly strict energy efficiency standards in automotive engines [7,21].

Provided such a complexity, it is difficult to consistently produce

* Corresponding author.
*E-mail address:* moschos.papananias@brunel.ac.uk (M. Papananias).

https://doi.org/10.1016/j.jmapro.2026.05.081
Received 8 October 2025; Received in revised form 27 April 2026; Accepted 27 May 2026
Available online 8 June 2026

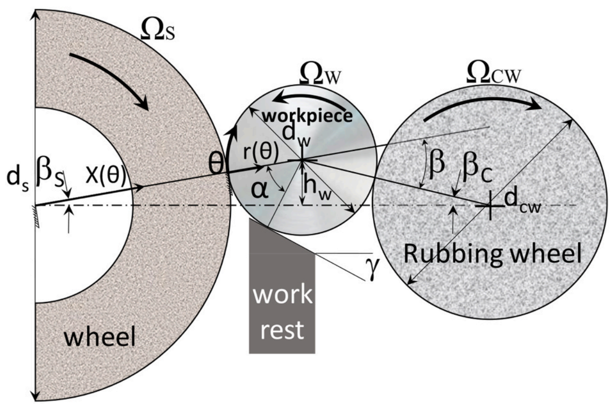


**Fig. 1.** Geometrical entities in centerless grinding.

precise roundness in a reliable, efficient, and scientifically controlled way. In particular, a reliable process parameters selection needs a model that is able to predict the resulting WP quality, allowing what-if analysis and optimization. The International Academy for Production Engineering (CIRP) keynote [8] provided a comprehensive review of the most widely used physical and empirical models for simulating key process outputs, such as grinding forces and power, surface integrity, surface finish, dimensional accuracy, and geometrical tolerances, taking into account the specific grinding energy and the wheel wear. A subsequent CIRP keynote in 2006 [9] expanded on this foundation by presenting the state of the art in grinding process modelling and simulation, discussing various approaches along with their capabilities, limitations, and emerging trends. Dealing specifically with centerless grinding, some time-domain simulation models have been developed for the investigation of WP profile generation [10–13]. However, the significant factors and their overall effects on the WP quality do not emerge clearly from such an implicit modelling approach; therefore, they do not provide an overall view on the relationship between the initial and the final profiles, as a function of the selected process setup. Besides, their open-loop construction implies the a priori accurate knowledge of several process parameters, while their identification from experiments can be carried out only by resorting to a time-consuming simulation-error approach.

Even when structural dynamics is not considered, geometric rounding mechanism entails a dynamic model, because the delayed spatial interactions introduce additional states (in the theoretical case of a continuous WP profile, the states form an infinite dimensional manifold): therefore, centerless grinding operations can be modelled by Delayed Algebraic Equations (DAEs). Unlike Delayed Differential Equations (DDEs), which are crucial when tackling self-excited vibrations in milling, turning and in-center grinding [14], these equations do not involve time derivatives of the unknown function (in our case, describing the discretized WP profile). Instead, they establish kinematic relationships between the function's values at different points in time, incorporating delay terms directly. The solution to DAEs often involves iterative methods or fixed-point methods since these equations are generally nonlinear. The primary challenge is handling delays in evaluating function values, especially when delays are not integer multiples of a chosen time step. Fortunately, the centerless grinding rounding mechanism gives rise to linear DAEs. In this case, when delays are fixed and the coefficients are constant, the equations can be arranged in a matrix form, equivalent to a linear or affine transformation. In [15], a transition matrix approach was applied to the stability analysis of milling processes, with the key focus on eigenvalues computation. A similar approach has been introduced in [16], treating the stability of multistage centerless grinding processes. In general, many works involve the discretization of the dynamical system entailed by the cutting process to carry out a stability analysis [17], but none exploit a discrete linear model to study the profile evolution, comprising the effect of the geometrical component produced by the nominal material removal.

The approach proposed herein consists of modelling the grinding process as a discrete linear dynamical system, so that each stage of the operation, e.g., roughing or finishing, can be described as an affine transformation operated by a constant transition matrix that embeds the linearized discrete process dynamics, and an offset component that reproduces the nominal material removal due to axis feed. Relying on an opportune state augmentation, the affine transformation includes a linear-phase low pass filter that reproduces the contact filtering effect due to wheels and WP engagement. The affine transformation can be built starting from a Physics-Based (PB) model of the process but also identified from grinding samples, by a purely Data-Driven (DD) approach, based on an over-determined linear system on the measured initial and final profiles, avoiding the measurement of additional process signals, not always available in an industrial context. The DD model, identified by measurements during a past production, can be useful to evaluate the effect of a new batch of initial profiles on the final WP quality, thus, enabling a cheap off-line quality test, as outlined in Fig. 2. In this work, the identification accuracy is evaluated relying on "virtual experiments" provided by a High-Fidelity (HiFi) non-linear process model.

The paper is structured as follows. In Section 2, the centreless grinding model is introduced, in terms of physical phenomena and proposed discretization, leading to the affine transformation representation. In Section 3, the mathematical properties of the affine transformation are pointed out and traced back to grinding operation characteristics and quality, thus being useful for parameters optimization/selection. Section 4 exploits the reduced order frequency-based representation to propose a DD approach to identify the affine transformation, based on initial and final WP profile measurements. Section 5 presents the numerical validation of the proposed approaches, investigating their operational limits. Section 6 is dedicated to the concluding remarks.

## 2. Modelling of centerless grinding

A vast literature on centerless grinding represents the process by a linear model in the time domain, with non-linear dependency on process parameters [4]. In these works, the shape of the cylindrical WP is defined by the actual radius reduction at the contact point between the grinding wheel and the WP (denoted by $r(\theta)$ in Fig. 1). The reduction is produced by the wheel-WP engagement, due to the relative displacement produced by the imposed feed and the structural deflection generated by the grinding force. In this study, only the static compliance is considered, i.e., the structural deflection is assumed to be in phase with the process force applied to the structure, while the ground truth data are obtained by a High-Fidelity model that reproduces also the machine structure dynamics. Further, given that the grinding wheel radius is much larger than the WP radius, short wavelength undulations are quickly reduced by the well know *contact filtering* effect.

In this model, hereinafter referred to as *Low-Fidelity* (LoFi) model, the radial reduction $r(\theta)$ is expressed w.r.t. coordinate $\theta$ as:

$$\begin{aligned} r(\theta) = k\, a(\theta) + r(\theta - 2\pi) = k(x(\theta) + K_1 r(\theta-\alpha) - (z_{cc} * K_2 r)(\theta - (\pi-\beta)) \\ - (z_{cs} * r)(\theta - 2\pi)) + (z_{cs} * r)(\theta - 2\pi) \end{aligned} \tag{1}$$

where (referring to Fig. 1 for symbols definitions)

- $a(\theta)$ is the actual depth of cut (or infeed)
- $\alpha = \pi/2 - \gamma - sin^{-1}(2h_w/(d_s + d_w))$
- $\beta = sin^{-1}(2h_w/(d_s + d_w))$
- $K_1 := \frac{\sin\beta}{sin(\alpha+\beta)}$, control wheel contact

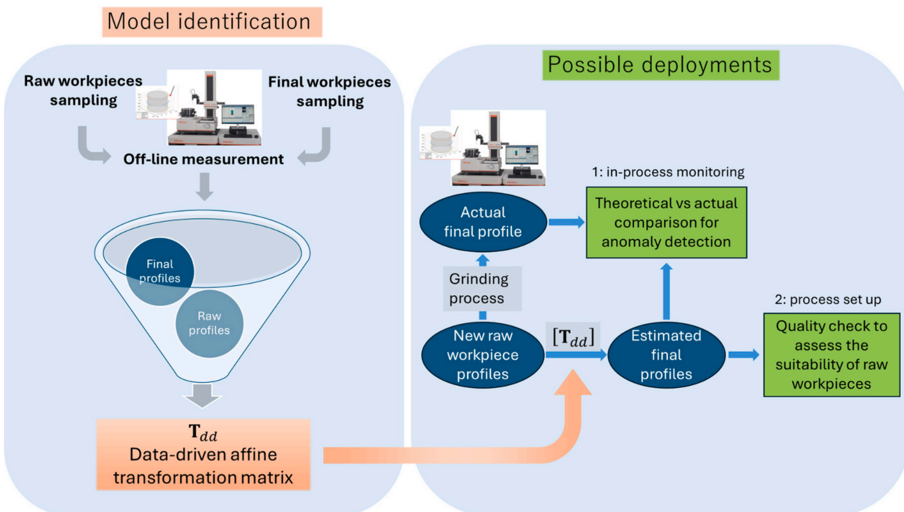


**Fig. 2.** Industrial application of the proposed data-driven centerless grinding model.

- $K_2 := \frac{\sin\alpha}{\sin(\alpha+\beta)}$, support blade contact
- $k$ is the so-called stiffness factor, i.e., the ratio between the nominal and actual depth of cut
- $x(\theta) = f_z\theta/2\pi$ is the commanded feed motion, which depends on the WP rotation angle $\theta$ and on the feed per revolution $f_z$
- $z_{cs/cc}(\eta)$ are the Finite Impulse Response (FIR) low-pass filters modelling the contact filtering effect at the operating wheel ($cs$) and the control wheel ($cc$) contact point, respectively.

Dealing with contact filtering, it has to be observed that the interference between the two bodies with finite dimensions is a complex and non-linear phenomenon [3] but, in order to quickly evaluate process stability, linearized contact filtering models have been proposed. Hashimoto [6] suggests describing contact filtering at both the control wheel/WP interface and the grinding wheel/WP shear interface, in the form of linear low-pass filters ($Z_{cc}$ and $Z_{cs}$). These filters are modelled in the wave-domain by zero-phase FIR filters, as discussed later in this section. While the filtering effect for the control wheel is realized by a low pass filter applied to the profile around the contact point, for the grinding wheel contact two different approaches have been considered. The first one is deduced from Hashimoto [6,18], taking into account that we consider only an overall static compliance, due to the machine and local compliances of the two wheel, as described in Section 3. The resulting model is depicted in Fig. 4, in the frequency domain (or, better, in the *waviness domain*). The low pass contact filter has as input the nominal infeed (denoted with $a_0$), while the output is used to compute the static deflection produced by the normal process force, named $a_{el}$. Then, the ratio between the nominal and actual depth of cut (i.e., *stiffness factor*) becomes frequency dependent, and can be expressed as follows:

$$k(n) := \frac{a}{a_0} = \frac{1}{1 + \frac{K_s}{K_{tot}} Z_{cs}(n)}$$

where $K_s$ is the so-called grinding stiffness [25], i.e., the ratio between the normal force ($F_n$) and the actual depth of cut, and in turn can be expressed starting from cutting specific energy ($E_v$) and the WP length ($b$), namely,

$$K_s := F_n \Big/ a = E_v b \frac{\Omega_w d_w}{\Omega_s d_s} \tag{2}$$

$K_{tot}$ is the overall relative stiffness between the operating wheel and the WP, defined as follows

$$K_{tot} := (1/K_c + 1/K_m)^{-1} \tag{3}$$

being $K_c$ the overall contact stiffness (series of the contact stiffnesses between the WP and the operating wheel ($K_{cs}$), and between the WP and the control wheel ($K_{cc}$), as illustrated in Fig. 3, approximating $\cos\beta_c$, $\cos\beta_s \approx 1$), and $K_m$ the relative machine stiffness between wheels hubs. According to Hertzian contact theory for cylindrical bodies, $K_{cs}$ and $K_{cc}$ can be considered as constants.

It can be observed that $k(n)$ starts at low frequency from $\frac{1}{1+\frac{K_s}{K_{tot}}}$, i.e., the well-known constant stiffness factor [4], and reaches the value 1 at high frequency. A unity equivalent stiffness factor corresponds to an infinitely stiff machine that, in a centered grinding operation, would instantaneously remove all WP waviness. In a centerless process, instead, the actual infeed depends also on the displacement of the WP center, named $c_{WP}$ in the block diagrams.

A waviness passing at the control wheel contact produces an infeed that, depending on the $\beta$ angle, can decrease or, instead, increase the waviness amplitude. Considering that the grinding wheel should anyhow attenuate high frequency waviness, an alternative model has

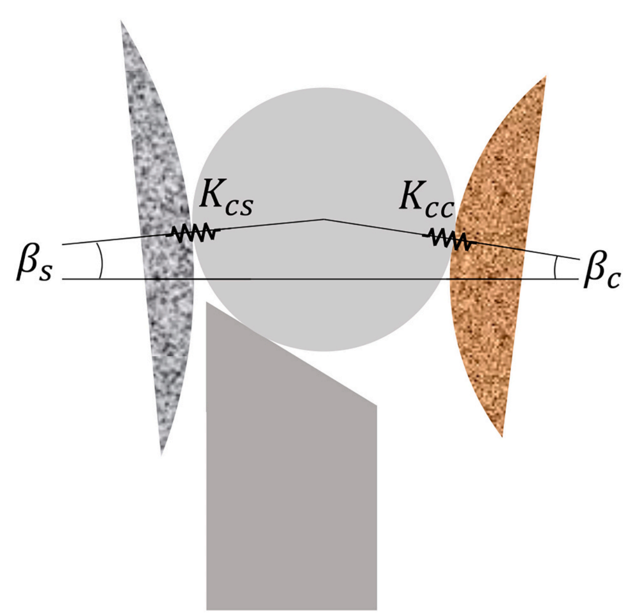


**Fig. 3.** Contact stiffnesses represented as lumped compliances.

been proposed, as described in Fig. 5. In this model the grinding wheel contact filter acts on the whole WP profile, before it undergoes material removal. A quantitative comparison between the two models is presented in Section 4.4, after model discretization.

According to Hashimoto et al. [6], the contact filter has the following frequency response:

$$Z_{cs/cc}(n) := \mathscr{F}\left(z_{cs/cc}(\eta)\right)(n) = \frac{1}{2}\left(1+\cos\left(\frac{l_{cs/cc}}{d_w}n\right)\right) \tag{4}$$

where $l_{cs/cc}$ is the length of the arc of contact between the wheels (grinding or control) and the WP, and $n$ is the number of waviness cycles around the profile (i.e., "waves per turn"). Please note that the Frequency Response Function (FRF) phase is identically null. The effect of both filters is discussed in Section 4.4.

The actual contact length $l_{cs}$, not explicitly defined in the reference work [6], depends both on geometrical factors and bodies compliance, according to the following relationship [4]:

$$l_{cs} = \sqrt{{l_{gs}}^2 + {l_{fs}}^2}$$

where $l_{gs}$ is the *geometric* contact length of the wheel-WP engagement, and $l_{fs}$ is the *deflective* component of the contact length due to the wheel-WP local deformation. The relevant literature [4] states that:

$$l_{gs} = \sqrt{a\left({d_w}^{-1} + {d_s}^{-1}\right)} \tag{5}$$

$$l_{fs} = \sqrt{C_s F_n\left({d_w}^{-1} + {d_s}^{-1}\right)} \tag{6}$$

where $F_n$ is the normal grinding force at the wheel-WP contact point and $C_s$ is a specific coefficient that depends on the wheel and WP materials, wheel roughness and contact width (basically the WP length $b$). According to [4]:

$$C_s = \frac{8R_f^2}{\pi b E^*}$$

where $R_f$ is the so-called roughness factor, which takes into account the fact that the contact occurs only on asperities and $E^*$ is the equivalent Young modulus of the operating wheel and WP pair, given by $E^* = \left(E_{ow}^{-1} + E_{wp}^{-1}\right)^{-1}$, where $E_{ow}$ and $E_{wp}$ are the Young modulus of operating wheel and WP materials, respectively.

On its turn, $F_n$ (at steady state) can be computed based on the volumetric specific energy $E_v$ [4] and the other process parameters, as done in Eq. (2). In the case of control wheel, given the null depth of cut, the contact length depends only on the deflective component:

$$l_{cc} = l_{fc} = \sqrt{C_c F_n\left({d_w}^{-1} + {d_{cw}}^{-1}\right)} \tag{7}$$

where $d_{cw}$ is the control wheel diameter and $C_c$ a specific coefficient, analogous to $C_s$ in Eq. (6).

### 2.1. Stiffness factor and contact filters identification

The parameters $C_s$, $C_c$ and $K_c$ appearing in Eqs. (6), (7) and (3) depend on complex constitutive laws and their theoretical estimation is affected by large uncertainties. On these premises, the nominal values $C_{s0}$, $C_{c0}$ and $K_{c0}$ [4] are adjusted by corresponding correcting factors $\delta_{C_s}$, $\delta_{C_c}$, $\delta_{K_c}$. They are estimated resorting to a simulation error approach that minimizes a loss function that considers the computed profiles error w.r.t. a reference grinding dataset, which in our case is provided by virtual experiments generated by a HiFi process model, borrowed from [19]. Namely, we solve

$$\{\delta_{K_c}, \delta_{C_s}, \delta_{C_c}\} = \arg\min_{\delta_{K_c}, \delta_{C_s}, \delta_{C_c}} L(\delta_{K_c}, \delta_{C_s}, \delta_{C_c} | \mathscr{D}) \tag{8}$$

where $\mathscr{D} := \left\{\left(\left(\check{\mathbf{r}}_0^i, \mathbf{p}_i\right), \check{\mathbf{r}}_{N_{r_i}}^i\right\}_{i=1,\dots,N_S}$ is the dataset of training reference profiles, with $\check{\mathbf{r}}_0^i$ the $i^{th}$ initial raw profile, $\mathbf{p}_i$ the vector of process parameters and $\check{\mathbf{r}}_{N_{r_i}}^i$ the final profile after $N_{r_i}$ WP revolutions generated by the HiFi model. According to the LoFi model of Eq. (1),

$$\mathbf{p}_i := \left\{h_{w_i}, f_{z_i}, d_{w_i}, \gamma_i, \Omega_{w_i}, N_{r_i}, Z_{cs}\left(\Omega_{w_i}, f_{z_i}, d_{w_i}\right), Z_{cc}\left(\Omega_{w_i}, f_{z_i}, d_{w_i}\right)\right\} \tag{9}$$

while $E_v$, $d_s$, $d_{cw}$, $K_m$, $K_{c0}$, $C_{s0}$, $C_{c0}$, $\delta_{K_c}$, $\delta_{C_s}$, $\delta_{C_c}$, $\Omega_s$ are considered fixed in $\mathscr{D}$. It can be observed that WP velocity $\Omega_{w_i}$ does not appear explicitly in Eq. (1), nor in the filters definition of Eq. (4), but it influences the value of $F_n$, which appears in Eqs. (6), (7) and (2).

The loss function $L$ in Eq. (8) is designed to account for two fundamental error components: one related to the final profile harmonics in the frequency domain, which determine the shape, and the other to the final roundness indicator, which is the most significant process performance measure:

$$L := w_{FFT}L_{FFT} + w_{RND}L_{RND}$$

where $L_{FFT}$ is the *Maximum Element-wise Hybrid Error* (MEHE [27]) between the Discrete Fourier Transform (DFT) of the target profile $\check{\mathbf{r}}_{N_{r_i}}^i$ and the corresponding predictions $\mathbf{r}_{N_{r_i}}^i = T_r\left(\check{\mathbf{r}}_0^i, |\mathbf{p}_i\right)$; $L_{RND}$ is the *Hybrid Error* (HybErr [27]) between $\check{\mathbf{r}}_{N_{r_i}}^i$ and the roundness[1] of $\mathbf{r}_{N_{r_i}}^i$; $w_{FFT}$ and $w_{RND}$ are weights to adjust the relative importance of the error components.

## 3. Discrete affine transformation model

The Eq. (1) is a linear delayed algebraic functional equation that can be discretized into an affine transformation. To do this, first of all, let the WP profile (defined by the radial reduction $r(\theta)$ w.r.t. an arbitrary ideal circle) be discretized in $M$ radial values as illustrated in Fig. 6, where

$$\Delta\theta := \frac{2\pi}{M}, M \in \mathbb{N}$$

is the angular step between two subsequent radii. For sake of simplicity, let the following notation be introduced:

$$\theta_i := i\Delta\theta, i \in \mathbb{N}$$

$$r^{(i)} := r(\theta_i)$$

$$x_i := x(\theta_i)$$

$$z_{cs/cc}(\eta_i) := z_{cs/cc}^{(i)}$$

In the same way, contact angles $\alpha$ and $\beta$ must be transformed as well into their discretized values, $\alpha_d$ and $\beta_d$ before computing the $K_1$ and $K_2$ factors:

$$m_1 = round\left(\frac{\alpha}{\Delta\theta}\right),\ m_2 = round\left(\frac{\pi-\beta}{\Delta\theta}\right),\ \alpha_d = m_1\Delta\theta,\ \beta_d = m_2\Delta\theta \tag{10}$$

To implement the contact filters described by Eq. (4), since a phase delay could lead to a fictitious process instability, zero-phase filters are adopted, realized by a FIR with linear phase delay, centred around the contact point between the wheel and the WP, i.e., $z_{cs/cc}(\eta) = z_{cs/cc}(-\eta)$, to get a null phase delay in the filter passband. Half of the filter must be applied to the original profile, on points that have already passed through the material removal process. To be able to do it, the corresponding radius values are stored in a buffer, as illustrated in Fig. 7.

[1] The roundness $R$ of a profile is the deviation from a perfect circle. For a discretized profile it is defined as: $R = \max_j r^{(j)} - \min_j r^{(j)}$.

Overall, Eq. (1) can be discretized as:

$$r(\theta) \cong r^{(i)} = k\left(x_i + K_1 r^{(i-m_1)} - K_2 \sum_{j=-N_{Fc}}^{N_{Fc}} z_{cc}^{(j)} r^{(i-j-m_2)} + \sum_{j=-N_{Fs}}^{N_{Fs}} z_{cs}^{(j)} r^{(i-j-M)}\right) + \sum_{j=-N_{Fs}}^{N_{Fs}} z_{cs}^{(j)} r^{(i-j-M)}, \quad \forall \theta \in [\theta_i, \theta_{i+1}]$$

where $\mathbf{z}_{cs} \in \mathbb{R}^{2N_{Fs}+1}$ and $\mathbf{z}_{cc} \in \mathbb{R}^{2N_{Fc}+1}$ are the coefficients vectors of the symmetric FIR filters modelling the contact filters respectively at the operating and control wheels contact points, as explained above. Then, the evolution of the WP profile $\mathbf{r}_n := \left[r_n^{(1)}, r_n^{(2)}, \dots, r_n^{(M)}\right]^T$ from a generic angular step $n$ to step $n+1$, is obtained by composing the update of the first element of $\mathbf{r}_n$ (which corresponds to the wheel-WP contact point) with a global circular shift that corresponds to a $\Delta\theta$ rotation of the WP. In compact form:

$$\widehat{\mathbf{r}}_{n+1} = \mathbf{G}\widehat{\mathbf{r}}_n + k\mathbf{u}(x_n + \Delta x) \tag{11}$$

where

$$\mathbf{u} := [1, 0, \dots, 0]_{1\times(M+2N_{Fs}+1)}^T$$

$$\widehat{\mathbf{r}}_n := \left[\mathbf{r}_n^T \;\mid\; \mathbf{s}_n^T\right]^T := \left[\mathbf{r}_n^T \;\mid\; r_{n-1}^{(1)}, r_{n-1}^{(2)}, \dots, r_{n-1}^{(N_{Fs})}\right]^T$$

where $\mathbf{s}_n$ is a profile *buffer* that contains the original value of points that already passed the grinding wheel contact point, required to apply the digital contact filter with zero mean delay (see Fig. 7). The setup of the $\widehat{\mathbf{r}}_n$ vector, starting from $\mathbf{r}_n$ and the reverse transformation can be realized by matrix multiplications:

$$\widehat{\mathbf{r}}_n = \begin{bmatrix} \multicolumn{2}{c}{\mathbf{I}_M} \\ \mathbf{I}_{N_{Fs}} & \mathbf{0}_{N_{Fs}\times M-N_{Fs}} \end{bmatrix} \mathbf{r}_n; \; \mathbf{r}_n = \begin{bmatrix} \mathbf{I}_M & \mathbf{0}_{M\times N_{Fs}} \end{bmatrix} \widehat{\mathbf{r}}_n$$

where $\mathbf{I}_M$ and $\mathbf{I}_{N_{Fs}}$ are identity matrices of size $M$ and $N_{Fs}$ respectively, and $\mathbf{0}_{N_{Fs}\times M-N_{Fs}}$ and $\mathbf{0}_{M\times N_{Fs}}$ are the null matrices of size $N_{Fs} \times M - N_{Fs}$ and $M \times N_{Fs}$, respectively.

Adopting a coherent notation and rearranging, the resulting profile transformation matrix, for a single processing step, is given by:

$$\mathbf{G} := \begin{bmatrix} \mathbf{0}_{1\times m_1} \; kK_1 \; \mathbf{0}_{1\times(m_2-m_1-N_{Fc}-1)} \; -\mathbf{z}_{cc}kK_2 \; \mathbf{0}_{1\times(M-m_2-N_{Fc}-N_{Fs}-1)} \; \mathbf{z}_{cs}(1-k) \\ \mathbf{I}_{M-1\times M-1} \qquad\qquad \mathbf{0}_{M-1\times 1} \end{bmatrix} \tag{12}$$

The Eq. (5) must be appended with the evolution of machine feed motion:

$$x_{n+1} = x_n + \Delta x \tag{13}$$

where $\Delta x$ is the feed motion per simulation step, defined as

$$\Delta x := f_z \frac{\Delta\theta}{2\pi}$$

The key elements of the discretized WP profile are represented in Fig. 7. Three indices are respectively associated with the material removal point ($i_s$) , the control wheel contact point ($i_c$), and the support blade contact ($i_b$). The filters coefficients $\mathbf{z}_{cs/cc}$ convolves the WP profile around $i_s$ and $i_c$.

Iterating Eqs. (11) and (13) from the initial state $\widehat{\mathbf{r}}_0$ to the final state $\widehat{\mathbf{r}}_n$, the overall (multistep) profile transformation becomes:

$$\begin{aligned} \widehat{\mathbf{r}}_n &= \mathbf{G}^n\widehat{\mathbf{r}}_0 + k\sum\nolimits_{j=0}^{n-1} \mathbf{G}^{n-1-j}\mathbf{u}(x_0 + (1+j)\Delta x) \\ &= \mathbf{G}^n\widehat{\mathbf{r}}_0 + k\sum\nolimits_{j=0}^{i-1} \mathbf{G}^{i-1-j}\mathbf{u}x_0 + k\sum\nolimits_{j=0}^{i-1} \mathbf{G}^{i-1-j}\mathbf{u}(1+j)\Delta x \end{aligned} \tag{14}$$

The last two addends of Eq. (14) are sums of matrix geometric series, which have a closed form expression; hence, Eq. (14) can be rewritten as:

$$\begin{aligned} \widehat{\mathbf{r}}_{n_1} &= T(\widehat{\mathbf{r}}_0) := \mathbf{G}^n\widehat{\mathbf{r}}_0 + k\,(\mathbf{I}-\mathbf{G})^{-1}(\mathbf{I}-\mathbf{G}^n)\,\mathbf{u}x_{0_1} \\ &\quad + k\,\left(\mathbf{I}-\mathbf{G}^{-1}\right)^{-2}\left[n\,\mathbf{G}^{-2} - (n+1)\,\mathbf{G}^{-1} + \mathbf{G}^{n-1}\right]\mathbf{u}\Delta x \end{aligned} \tag{15}$$

It can be observed that $T: \mathbb{R}^{N_d+N_{Fs}} \longrightarrow \mathbb{R}^{N_d+N_{Fs}}$ is an affine transformation, where the additive part is due to feed motion $\Delta x$. Through coefficients $K_1$, $K_2$, $k$, $\Delta x$ and filters $\mathbf{z}_{cs/cc}$, the transformation $T$ nonlinearly depends on process parameters, which can be grouped in the parameters vector $\mathbf{p}$, already defined in Eq. (9). If necessary, this dependency will be denoted by $T(\widehat{\mathbf{r}}_0|\mathbf{p})$.

It is worth noting that the depth of cut $a(\theta)$ in Eq. (1) can never become negative due to its physical meaning. This constraint is not considered in the linear transformation $T$, entailing a relevant approximation of the affine approach if a wheel-WP detachment occurs, as it can happen during the initial approach to the WP and during unstable operations. In order to minimize air cutting limit this effect, the initial position $x_0$ must be set to have the grinding wheel and WP touch each other. The possible effect of detachment is discussed in Section 6.2.

A centerless grinding operation is usually composed by multiple stages (e.g., for roughing, finishing and spark-out) characterized by different process parameters (essentially feed rate, which is null in the case of spark-out, even if more complex multi-stage approaches are possible [16]). The change in grinding force modifies the elastic deformation and, therefore, the contact length at the grinding wheel. As a consequence, the stiffness factor $k$ in Eq. (15) undergoes an instantaneous change that, because of Eq. (15), would provoke a step in the WP profile, while, in reality the machine undergoes a smooth transient elastic displacement due to the progressive change in grinding force. Such a transient is not modelled by the proposed transformation approach: for each stage the model assumes a unique structural deformation, equal to the steady state value dependent on the stiffness factor for that stage. To avoid this unrealistic effect, the initial $x_0$ position is adjusted at each stage commutation by equating the effective displacements at the beginning of the new stage and at the end of the previous stage, i.e.,

$$x_{0,j} = \frac{k_{j-1}}{k_j}\left(x_{0,j-1} + N_{r_{j-1}}\,\Delta x_{j-1}\right)$$

where $x_{0,i}$ is the value to be attributed to $x_0$ at the beginning of stage $i^{th}$, $k_j$ and $k_{j-1}$ are the stiffness factors associated with stages $j^{th}$ and $(j-1)^{th}$ respectively, $N_{r_{j-1}}$ and $\Delta x_{j-1}$ denote the number of steps and the feed per step of stage $(j-1)^{th}$. Then, the profile evolution of one stage can be iteratively computed starting from the previous one:

$$\widehat{\mathbf{r}}_{n_j} = \mathbf{G}^{(n_j-n_{j-1})}\widehat{\mathbf{r}}_{n_{j-1}} + k\,(\mathbf{I}-\mathbf{G})^{-1}\left(\mathbf{I}-\mathbf{G}^{(n_j-n_{j-1})}\right)\mathbf{u}x_{0,j}$$

## 4. Properties of the transition matrix

The affine transformation model enables the direct mapping of physical process phenomena onto the corresponding profile transformations, thereby facilitating process analysis and optimization. This chapter examines these fundamental properties through examples based on the 2-stage grinding process (roughing, with linear feed axis motion, and spark-out, with fixed feed axis) described by the parameters of Table 1:

Applying Eq. (5) – Eq. (7) to the process parameters in Table 1, the contact lengths between the WP and, respectively, the grinding and control wheels are computed: $l_{cs} = 0.72mm$ and $l_{cc} = 0.35mm$. The target filter frequency responses, given by Eq. (4), are used to design the Finite Response filters by the Matlab fir2 function, considering respectively a filter order of 54 and 30.

**Table 1**
Grinding process parameters.

| Parameter | Value | Unit |
|---|---|---|
| $h_w$ | 8 | mm |
| $f_z$ | 15 | μm |
| $\gamma$ | 20 | ° |
| $d_w$ | 36 | mm |
| $d_s$ | 610 | mm |
| $d_{cw}$ | 355 | mm |
| $\Omega_{WP}$ | 3.2870 | rps |
| $N_r$ | 10 | – |
| $N_{r_{spark-out}}$ | 2.5 | – |
| $M$ | 1800 | |

### 4.1. Eigenvalues and eigenvectors after more than one processing step

In typical grinding simulations the profile is discretized in the angular domain with $M = 1000$–$4000$ points while the process lasts 10–30 WP turns. Therefore, the application of the affine transformation from Eq. (15) requires the elevation of a $\mathbf{G}$ matrix containing from 1 to 16 millions of elements to a power of 10,000–130,000. This operation is typically ill conditioned. To avoid large numerical approximations, an eigen-decomposition is applied, exploiting then the matrix power rule:

$$\mathbf{G}^i = \mathbf{\Phi}\,\mathbf{\Lambda}^i\mathbf{\Phi}^{-1},$$

where $\mathbf{\Lambda}$ is a diagonal matrix with $\mathbf{G}$ eigenvalues on the main diagonal and $\mathbf{\Phi}$ contains the corresponding eigenvectors.

Therefore, when several processing steps are performed, the eigenvectors remain unmodified, preserving the structure described in Section 4.3. For the eigenvalues, instead, if they are stable the modulus decreases, while, if an eigenvalue is unstable, it increases, producing the typical exponential growth of the waviness. The eigenvalues phase also linearly increases, spreading the eigenvalues around the unit circle in the complex plane. The relationship between *eigenvalue phase* and *waves per turn* in the corresponding eigenvector is therefore lost because the eigenvalue phase can travel several turns around the unitary circle, producing an aliasing effect. It can be shown (see Appendix A) that there is at least one marginally stable eigenvalue, i.e., with unitary modulus. If no unstable eigenvalues are present, the marginally stable eigenvalues determine the steady state profile shape, which results in a combination of harmonic components: they are originated both from the initial WP profile and from the nominal material removal due to feed motion (produced by the terms that are multiplied by $\mathbf{G}^n$ in Eq. (15). In general, such harmonic components yield an *almost* integer number of waves per turn that induce profile waves with limited precession during process execution.

### 4.2. Profile transformation in the frequency domain

It is well known in the literature that a centerless grinding process can be kinematically unstable [1] and produce WPs with a significant periodic undulation. It is therefore of interest to evaluate the obtained profile in terms of waviness components, applying the Fourier transform on the WP profile:

$$\mathbf{r}_i = \mathbf{F}\mathbf{c}_i \tag{16}$$

where each column $m$ of $\mathbf{F}$ contains the complex harmonics $F_{p,m} = \left(1/\sqrt{M}\right)e^{j\frac{2\pi mp}{M}}$, while $p$ increases along the WP profile. The harmonic shapes are scaled to get a unitary $\mathbf{F}$ matrix; $\mathbf{c}_i$ contains the corresponding complex coefficients for the profile at the $i^{th}$ step. The complex coefficients entail the correct preservation of the phase of the harmonic components, which is necessary to represent exactly both the profile geometry and the WP initial angular position. In fact, it can be shown that the initial angular position has an effect on the final profile, above all in the case of short operations (i.e., few WP revolutions).

Substituting Eq. (16) in Eq. (15) and, taking into account that $\mathbf{F}$ is a unitary matrix, pre-multiplying by $\mathbf{F}^T$ gives:

$$\mathbf{c}_i = \mathbf{F}^T\mathbf{G}^i\mathbf{F}\,\mathbf{c}_0 + k\,\mathbf{F}^T(\mathbf{I}-\mathbf{G})^{-1}\left(\mathbf{I}-\mathbf{G}^i\right)\mathbf{u}x_0 + k\mathbf{F}^T\mathbf{G}^i\left(\mathbf{I}-\mathbf{G}^{-1}\right)^{-2}\left[i\,\mathbf{G}^{-i-2} - (i+1)\,\mathbf{G}^{-i-1} + \mathbf{G}^{-1}\right]\mathbf{u}\Delta x$$

The $\mathbf{G}_F^i \equiv \mathbf{F}^T\mathbf{G}^i\mathbf{F}$ matrix defines how the spectral components of the initial profile are transformed into the spectral components of the profile at step $i^{th}$. The next section discusses the structure of $\mathbf{G}_F^i$.

### 4.3. Eigenvectors of the linear mapping and transformation matrix in the frequency domain

The matrix $\mathbf{G}$ in the affine transformation relates the actual profile to the profile at the previous step, representing the autonomous part of the discrete system dynamics. To analyse the affine transformation, it is useful to characterize the eigenvalues and eigenvectors of the transformation matrix. The $\mathbf{G}$ matrix is composed of a generically non-zero first row, reproducing the material removal process, while all other rows of the matrix just shift the rest of the profile by one step (counter clockwise). This qualifies $\mathbf{G}$ as a *companion matrix,* in row form (while the transition matrix after $i$ steps is no longer a *companion matrix*). Usually, in standard companion matrices, the polynomial coefficients are stored in the last row: our form of companion matrix, with the polynomial coefficients located in the first row, is also defined as in *canonical form*. Given the properties of companion matrices, naming $\lambda_k := p_k e^{j\psi_k}$ the eigenvalues of $\mathbf{G}$, the corresponding eigenvectors are given by:

$$\mathbf{\Phi}_k = \nu_k\begin{bmatrix} 1 & \lambda_k^{-1} & \dots & \lambda_k^{-(M-1)}\end{bmatrix}^T$$

where $\nu_k$ is the usual free normalization parameter. The eigenvector exhibits therefore an exponential evolution along the WP profile:

$$\mathbf{\Phi}_k = \nu_k\left[\lambda_k^{-m}\right] = \nu_k\left[e^{g_k m}\right] \text{ for } m = 0, 1, \dots, M-1,$$

$$\text{with } g_k = -log(\lambda_k) = -log(p_k) + j(\psi_k + 2n\pi) \tag{17}$$

Let's compute, by Eq. (17), the last value of eigenvector $k$, for $m = M-1$:

$$\phi_{km} = p_k^{-(M-1)}e^{-j(M-1)\psi_k}$$

The corresponding number of waves per turn, $w$, is:

$$w = \frac{M-1}{2\pi}\psi_k$$

Therefore, the phase of the eigenvalues of $\mathbf{G}$ is proportional to the number of waves per turn in the corresponding eigenvector.

Let's consider the analytical Fourier transform of the exponential function in Eq. (17), over an infinite domain:

$$\mathbf{\Phi}_k(\omega) = \frac{\nu_k}{real(g_k) + j(\omega - imag(g_k))} = \frac{\nu_k}{-log(p_k) + j(\omega - \psi_k - 2n\pi)} \tag{18}$$

If an eigenvalue $\lambda_k$ is at the stability limit, i.e., $p_k = 1$, the corresponding eigenvector Eq. (17) is an undamped harmonic function. The corresponding $\mathbf{\Phi}_k(\omega)$, in (18) has a strong localized peak at $\psi_k + 2n\pi$. On the contrary, if the modulus of $\lambda_k$ is far from 1, i.e., the eigenvalue is strongly stable or unstable, the peak in the spectrum is spread on a larger frequency range. As a consequence, the eigenvectors of eigenvalues near the stability limit, being *near* undamped harmonic functions, are *almost orthogonal* to each other.

More in detail, when transforming the $\mathbf{G}$ matrix into the frequency domain $\mathbf{G}_F$, the Fourier series is computed over a finite interval, corresponding to one turn. As usually done in signal processing, the Fourier Transform of an eigenvector can be obtained by convolving the spectrum of the infinite exponential function, i.e., Eq. (18), with the spectrum of a rectangular window of duration one turn. The signal power is therefore diffused on some nearby spectral lines, by the so-called leakage effect, also for marginally stable eigenvalues.

The Fig. 8 shows, for the sample process, the spectrum, in modulus, of some complex eigenvectors. They are sorted by the modulus of the corresponding eigenvalue, from the largest (the first eigenvalue, equal to 1, as this process is stable) to the smallest (eigenvalue number 3654, equal to 0.687, in this example). As expected, the width of the peak increases when the eigenvalue gets far, in modulus, from 1.

Those remarks have an impact on the structure of the transition matrix in the frequency domain. Exploiting the eigenvector/eigenvalue decomposition:

$$\mathbf{G}^i = \mathbf{\Phi}\,\mathbf{\Lambda}^i\mathbf{\Phi}^{-1}, \qquad \mathbf{G}^i_F = \mathbf{F\Phi}\,\mathbf{\Lambda}^i\mathbf{\Phi}^{-1}\mathbf{F}^{-1} = \mathbf{F\Phi}\,\mathbf{\Lambda}^i(\mathbf{F\Phi})^{-1} \tag{19}$$

where $\mathbf{F\Phi}$ represents the Fourier series of the eigenvector, i.e., the $[\mathbf{\Phi}_k]$ previously computed. If $\mathbf{F\Phi}$ is a diagonal matrix also $\mathbf{G}^i_F$ is a diagonal matrix, i.e., each frequency component of the final profile depends only on the corresponding frequency component in the initial profile. The exposed eigenvalue/eigenvector analysis explains why, for the adopted example, $\mathbf{G}^i_F$ has an almost diagonal structure, shown in Fig. 9, with some limited coupling between nearby harmonic components.

Additionally, the matrix shows the well-known property that, depending on the adopted WP height, the process has a very different amplification for the odd and even frequency components [18], as further elaborated in the following section.

Given the almost diagonal structure of the process matrix in the frequency domain, it's convenient to adopt this approach to better analyse the process, evaluating its gains as a function of the frequency of the various waviness components. This encourages the adoption of reduction techniques in the frequency domain, to efficiently simplify WP profile description. This approach will be adopted in Section 5, for the DD process model identification. The residual coupling between different harmonics is exemplified in Section 6.2.

### 4.4. Eigenvalues of the linear mapping

Provided that the transition matrix $\mathbf{G}$ basically performs a one-step rotation of the discretized WP profile, with a small material removal lumped in a single contact point, it is not very different from a unitary circulant matrix [32]. Consequently, most eigenvalues have a modulus near to one. The corresponding eigenvectors, as explained in the previous section, are similar to undamped harmonic functions, with very localized frequency content. In this scenario the modulus of the eigenvalues quantifies the gain of the process at that frequency, similarly to the information given, in linear dynamical systems, by an FRF, even if, in this case, there is a partial coupling between different wavelengths. This gain is related to the considered process duration, i.e., to a given number of iterative steps.

Leveraging those remarks, a plot of the eigenvalue's modulus, referred to the eigenvalue frequency (deduced by its phase), gives an interesting overall view on process dynamics, directly quantifying how a harmonic component in the initial WP profile is attenuated or amplified in the final profile. As discussed in the previous section, this plot is incomplete because it does not show the existing coupling between different harmonics, especially when the eigenvalues are far from the unitary circle. For example, Fig. 10 characterizes different solutions to implement contact filters, described in Section 2, applied to the test process defined in Section 4:

A) No contact filters. Some eigenvalues have modulus higher that one, indicating an instable process;
B) One contact filter at the grinding wheel contact point, as depicted in Fig. 5, but without the filter at the control wheel contact. The system is now stable but a branch of eigenvalues still has a higher gain;
C) Contact filters at both the grinding and control wheel, as in Fig. 5;
D) Contact filter only at the grinding wheel, by the scheme proposed by Hashimoto. As in Fig. 4, but without the filter at the control wheel;
E) Contact filters at both the grinding and control wheel, as proposed by Hashimoto and depicted in Fig. 4.

In both cases, when at least one contact filter is implemented, a global decreasing trend appears in correspondence of the bandwidths of the adopted filters.

Before analysing the different models, it is useful to further investigate the type of information delivered by the plot, in particular the structure shown at low frequency, inside the bandwidth of the contact filters.

To study it, let's make the usual process stability analysis with the Nyquist criterion applied on the characteristic equation (Eq. 13.16 of reference [4]). Fig. 11 (a) illustrates the real part of $1 + \mathbf{G}_{open\ loop}$ function: when it assumes negative values, the closed loop system can be unstable. This correctly corresponds, in Fig. 11 (b), to the location of the eigenvalues of the transition matrix: an unstable system shows a $1 + \mathbf{G}_{open\ loop}$ function that goes down toward negative values and, correspondingly, transition matrix eigenvalues with modulus reaching, and possibly bypassing, the value of one. In our case only the one per turn component reaches a unity modulus, because the adopted test process is stable (with GW and CW contact filters). As predicted by the theory of geometrical stability in centerless grinding, the eigenvalues are near to integer number of waves per turn, with a clear amplitude difference between even and odd frequencies, expressed in waves per turn.

We can now go back to Fig. 10, to compare the various models:

A) with the Hashimoto approach without the Control Wheel filter (model D) a branch of the eigenvalues remains high, showing model instability. On the contrary, with the proposed approach (model B), the whole profile is filtered, producing some amplitude reduction on all eigenvalues. This effect has been preferred, because, given the large grinding wheel radius, high frequency waviness on the WP is always reduced;
B) When both the GW and CW filters are adopted, both approaches (models C and E) give similar results.

Based on those remarks, the modelling approach C, with a filter at the control wheel and the grinding wheel filter on the profile delayed by one turn, has been adopted in the following of this paper. The filter on the profile delayed by one turn attenuates the waviness even when there is no actual material removal (i.e., when grinding wheel / WP detachment occurs), producing a non-physical effect. But the overall effect is negligible because the proposed affine model must anyhow be applied when detachment is limited, given the linearity of the adopted LoFi approach.

## 5. Data-driven identification of the affine transformation

The proposed approach allows one to build, from traditional process models, an affine transformation that directly links, for fixed process conditions, the initial and final WP profiles. In this section, we investigate the possibility of learning the same model structure relying only on the initial and final profiles that are normally available also in industrial contexts.

Let $\boldsymbol{i}_j \in \mathbb{R}^{N_f}$ denote the vector of $N_f$ input features (e.g., initial profiles represented in the angular or frequency domains) and $\boldsymbol{o}_j \in \mathbb{R}^{N_f}$ the corresponding output features for the experiment $j = 1,2, \ldots, N_e$, under identical process parameters, including the feed per turn and number of turns. The number of features $N_f$ in the frequency domain depends on

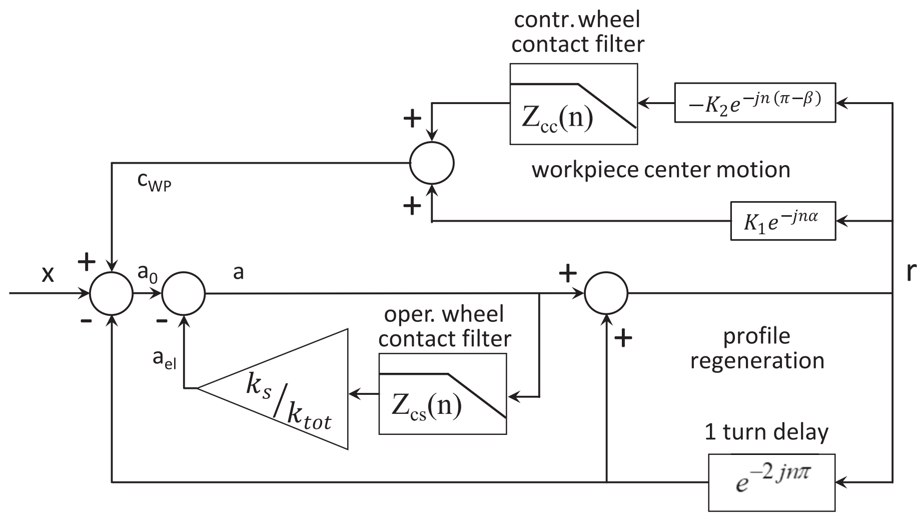


**Fig. 4.** Schematic of the process model with the grinding wheel contact filter modelled as in Hashimoto [18].

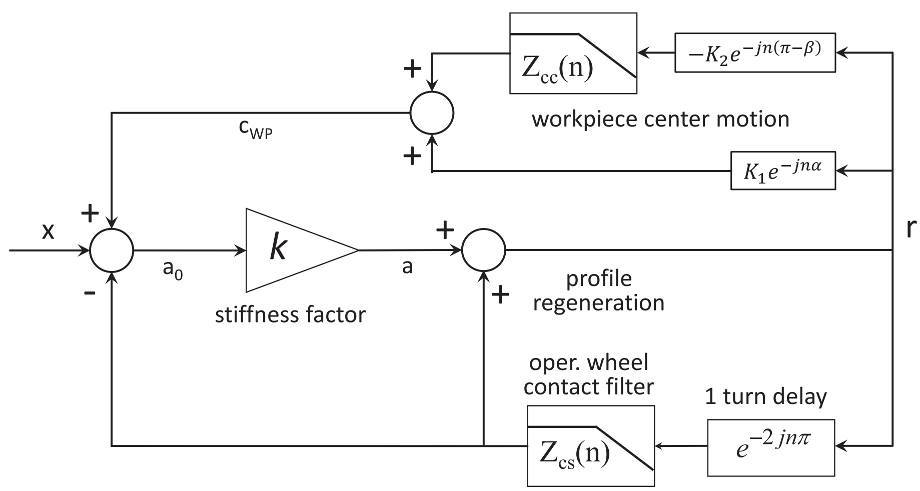


**Fig. 5.** Schematic of the process model with two contact filters (LoFi model).

the relevant harmonic content that is to be preserved in the profile description (as it has already mentioned at the end of Section 4.3 and will be exemplified in Section 6.3), which anyway cannot overcome half of the number of samples used in the discretization, according to Shannon theorem, to avoid aliasing.

Recalling the analytical relationship of Eq. (14), we assume that the relationship between input and output is governed by an affine transformation:

$$\boldsymbol{o}_j = \mathbf{G}_{dd}\, \boldsymbol{i}_j + \mathbf{c}_{dd} \tag{20}$$

where

- $\mathbf{G}_{dd} \in \mathbb{R}^{(N_f \times N_f)}$ is the empirical DD transition matrix;
- $\mathbf{c}_{dd} \in \mathbb{R}^{(N_f \times 1)}$ are the overall empirical DD bias coefficients of the affine transformation (translation component).

Resorting to an *augmented matrix* [28], Eq. (20) can be cast into a linear transformation as follows:

$$\boldsymbol{o}_j = \mathbf{T}_{dd} \begin{bmatrix} \boldsymbol{i}_j \\ 1 \end{bmatrix} \tag{21}$$

with $\mathbf{T}_{dd} := [\, \mathbf{G}_{dd}\, \mathbf{c}_{dd} \,] \in \mathbb{R}^{(N_f \times (N_f+1))}$ (augmented matrix).

To ensure robustness with respect to overfitting, we aggregate data across multiple $N_e$ experiments; then, Eq. (21) can be written $\forall j = 1, 2, \ldots N_e$ and assembled in the following overall system:

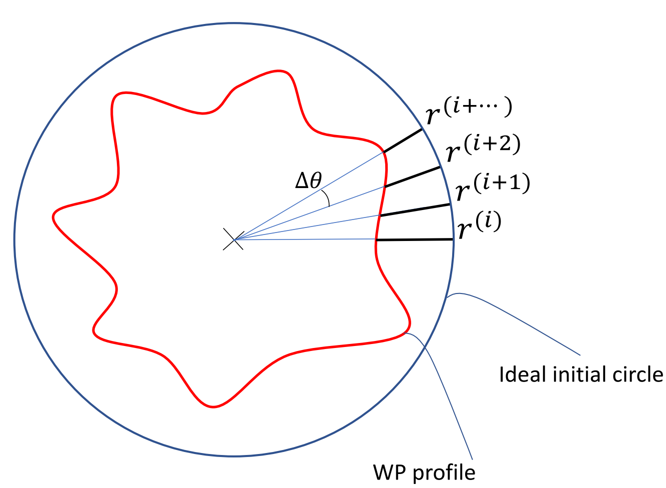


**Fig. 6.** Definition of the z-buffer profile: the elements represent the reduction of workpiece rays with respect to an ideal circular workpiece.

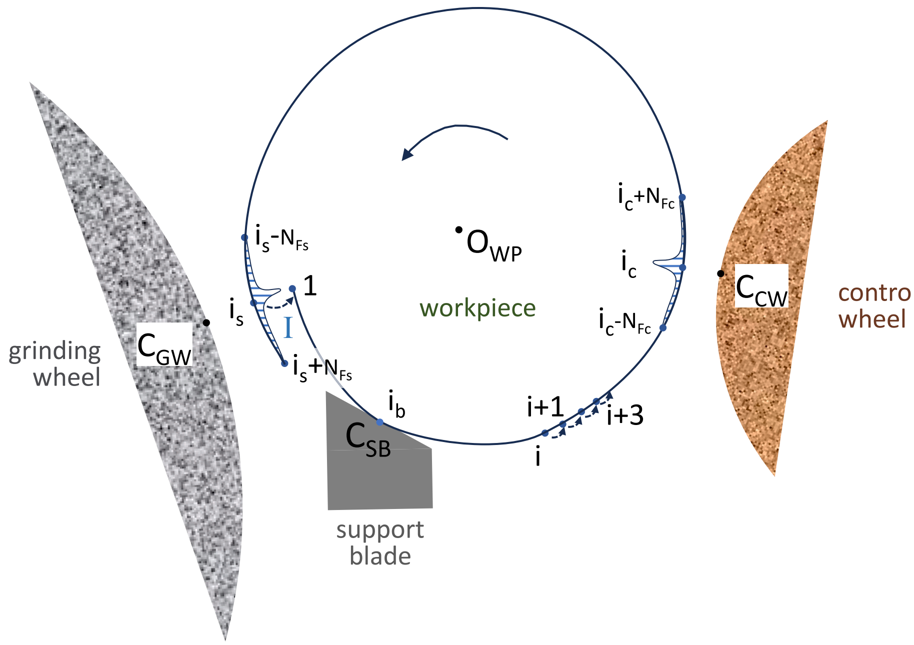


**Fig. 7.** Workpiece profile vector definition with the significant indices at the contact points between the workpiece and the grinding wheel (GW), the control wheel (CW) and the support blade (SB).

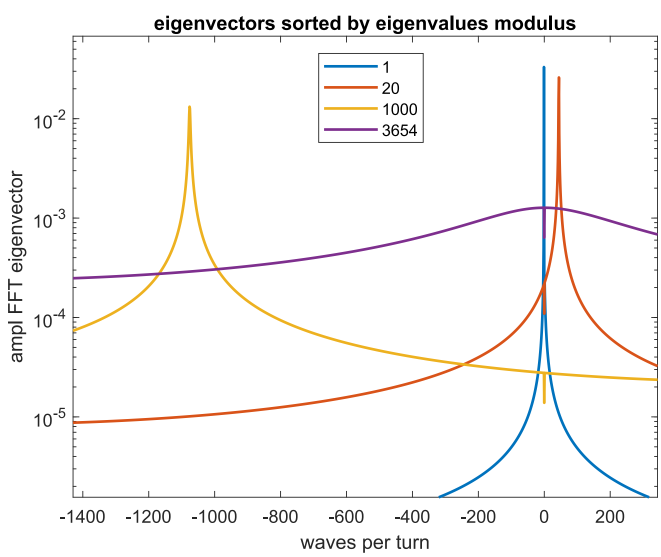


**Fig. 8.** Fourier Transform (modulus) of the eigenvectors of the transition matrix, sorted by the distance from 1 of the modulus of the corresponding eigenvalue. When the eigenvalue modulus is near to 1, the spectrum is more localized in the frequency domain.

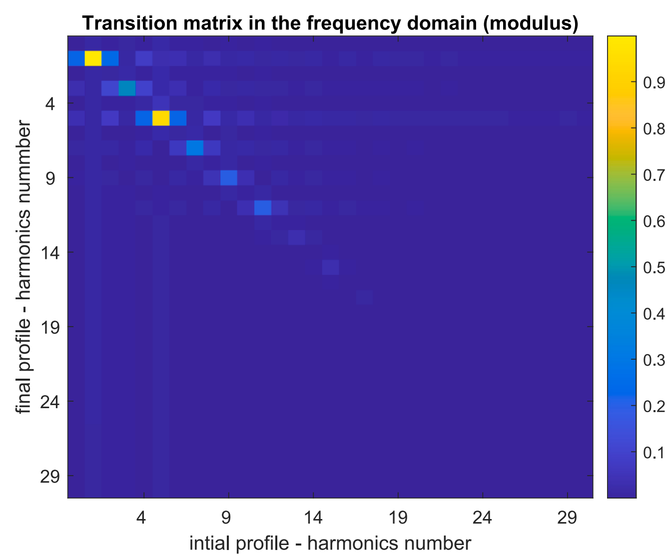


**Fig. 9.** Transition matrix in the frequency domain for adopted example.

$$\mathbf{O} = \mathbf{T}_{dd}\,\mathbf{A} \tag{22}$$

with

$$\mathbf{O} := \begin{bmatrix} \boldsymbol{o}_1 & \boldsymbol{o}_2 & \cdots & \boldsymbol{o}_j & \cdots & \boldsymbol{o}_{N_e} \end{bmatrix} := \begin{bmatrix} o_{11} & o_{12} & \cdots & o_{1N_e} \\ o_{21} & o_{22} & \cdots & o_{2N_e} \\ \vdots & \vdots & \ddots & \vdots \\ o_{N_f1} & o_{N_f2} & \cdots & o_{N_fN_e} \end{bmatrix} \in \mathbb{R}^{(N_f \times N_e)}$$

$$\mathbf{A} := \begin{bmatrix} \boldsymbol{i}_1 & \boldsymbol{i}_2 & \cdots & \boldsymbol{i}_j & \cdots & \boldsymbol{i}_{N_e} \\ 1 & 1 & \cdots & 1 & \cdots & 1 \end{bmatrix} = \begin{bmatrix} i_{11} & i_{12} & \cdots & i_{1N_e} \\ i_{21} & i_{22} & \cdots & i_{2N_e} \\ \vdots & \vdots & \ddots & \vdots \\ i_{N_f1} & i_{N_f2} & \cdots & i_{N_fN_e} \\ 1 & 1 & 1 & 1 \end{bmatrix} \in \mathbb{R}^{((N_f+1)\times N_e)}$$

Then, exploiting Eq. (22), we can compute an estimate of the affine augmented matrix $\mathbf{T}_{dd}$ using a *Ridge* regression approach, which belongs to the family of *regularized least squares* methods and entails the solution of the following minimization problem:

$$\widehat{\mathbf{T}}_{dd} = \arg\min_{\mathbf{T}_{dd}} \|\mathbf{O} - \mathbf{T}_{dd}\mathbf{A}\|_2^2 + \eta \|\,\mathbf{G}_{dd}\,\|_2^2 \tag{23}$$

where $\eta$ is a hyperparameter that modulates the matrix elements

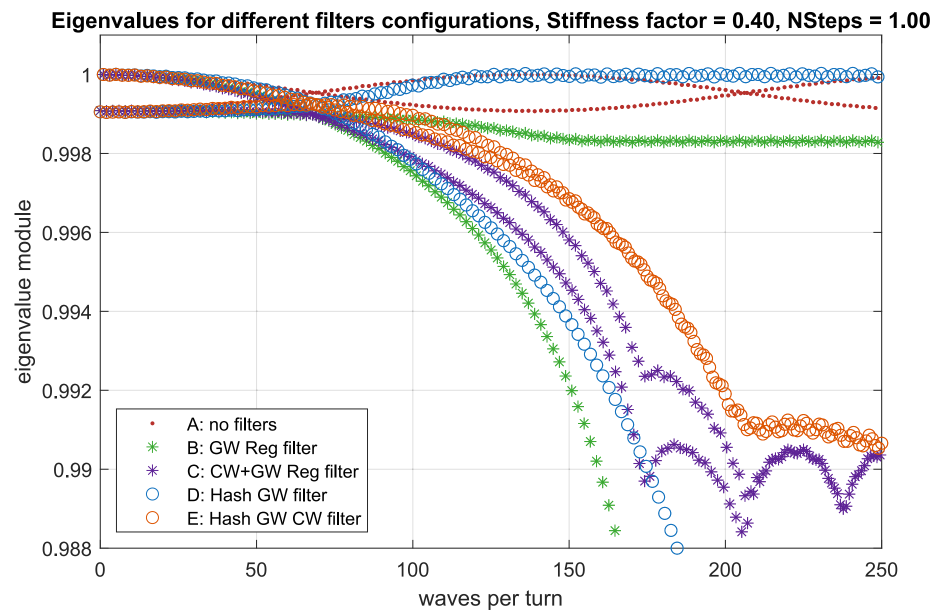


**Fig. 10.** Eigenvalues of the transition matrix for different examined contact filters configurations.

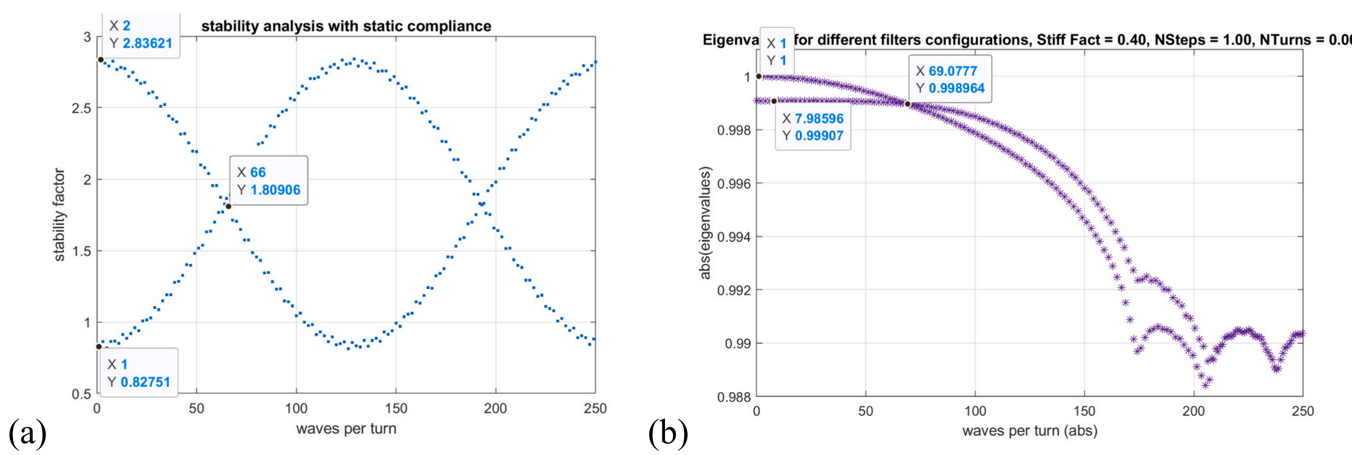


**Fig. 11.** (a): Real part of the open loop frequency response, used for the classic stability analysis. (b): Transition matrix eigenvalues (zoom of Fig. 10 (a)) for the system with filters on the control wheel and on the previous profile, at the grinding wheel.

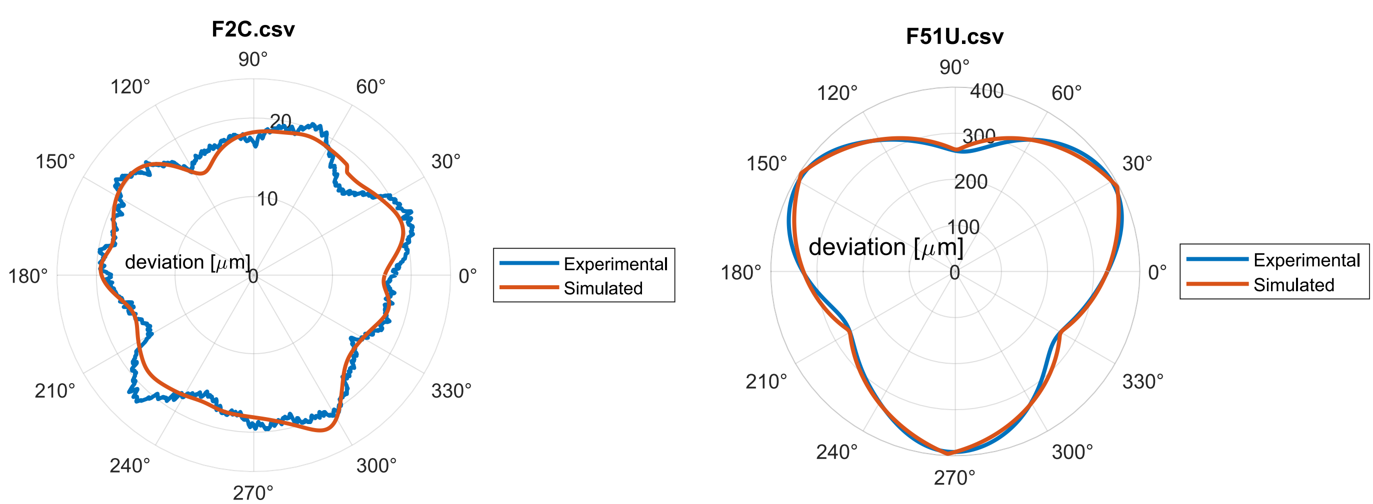


**Fig. 12.** Comparison between experimental and predicted workpiece profiles for a slightly unstable process (left) and a severely unstable process, dominated by a 3-lobes shape (right).

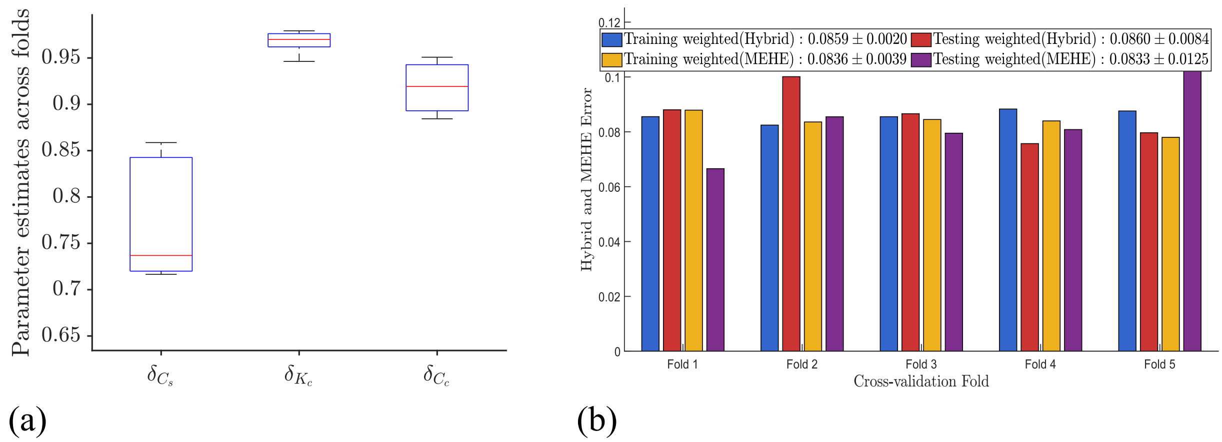


**Fig. 13.** (a). Boxplot of parameter estimates across folds; Fig. 13 (b). Cross-validation results for the physics-based affine transformation model. The bar plots report the HybErr (geometrical profile roundness) and the MEHE (profile spectrum) for both training and testing folds across $K = 5$ folds.

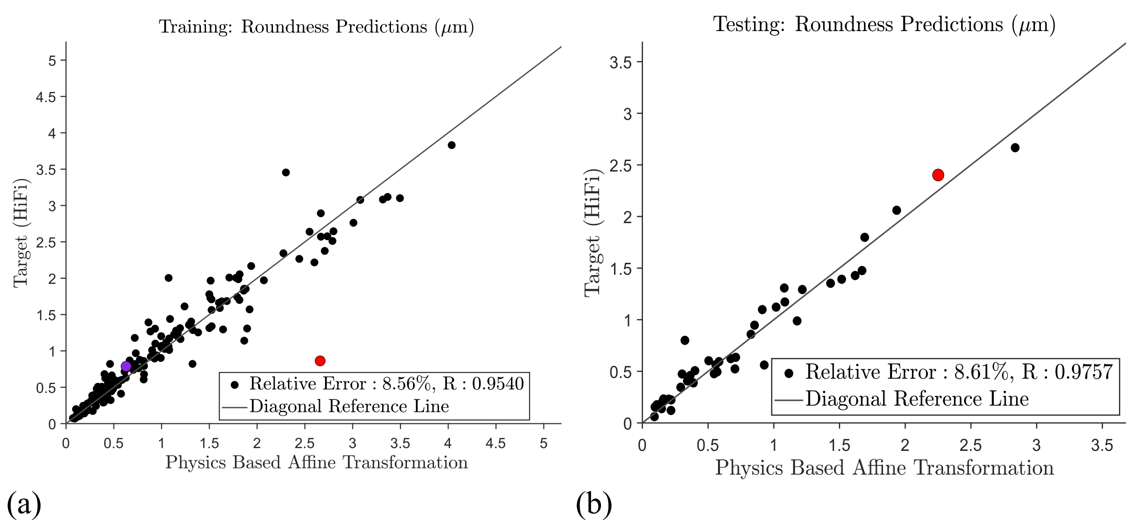


**Fig. 14.** Roundness predictions for Fold 3 of the $K$-fold cross-validation (a) training, (b) testing. The experiments corresponding to violet and red dots have been highlighted for reference in subsequent analysis. (For interpretation of the references to colour in this figure legend, the reader is referred to the web version of this article.)

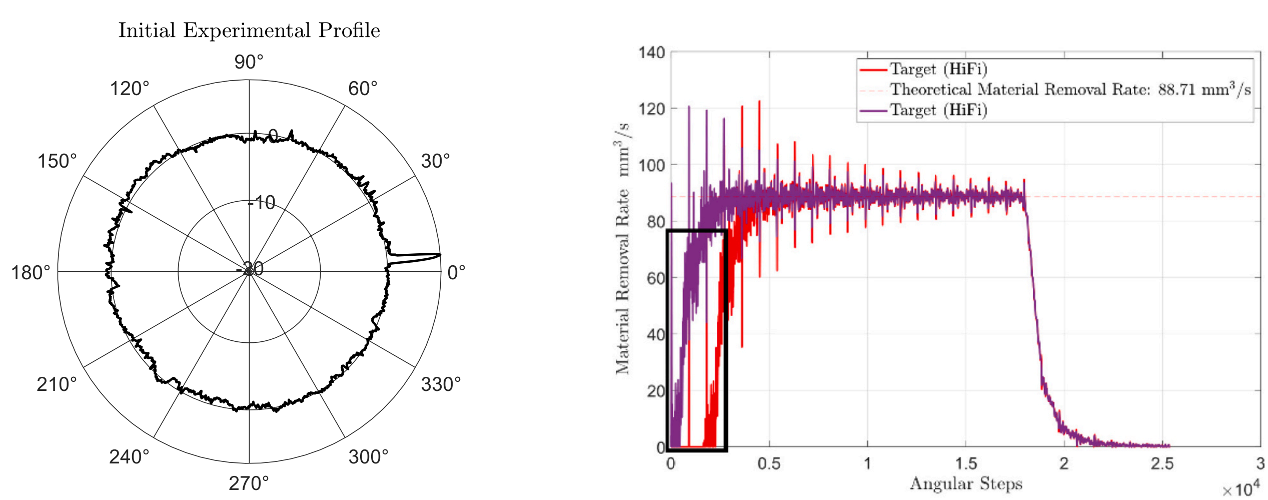


**Fig. 15.** Material removal rate predicted by the ground truth model (High-Fidelity) for the two training samples highlighted respectively in violet and red in Fig. 14 (a). (For interpretation of the references to colour in this figure legend, the reader is referred to the web version of this article.)

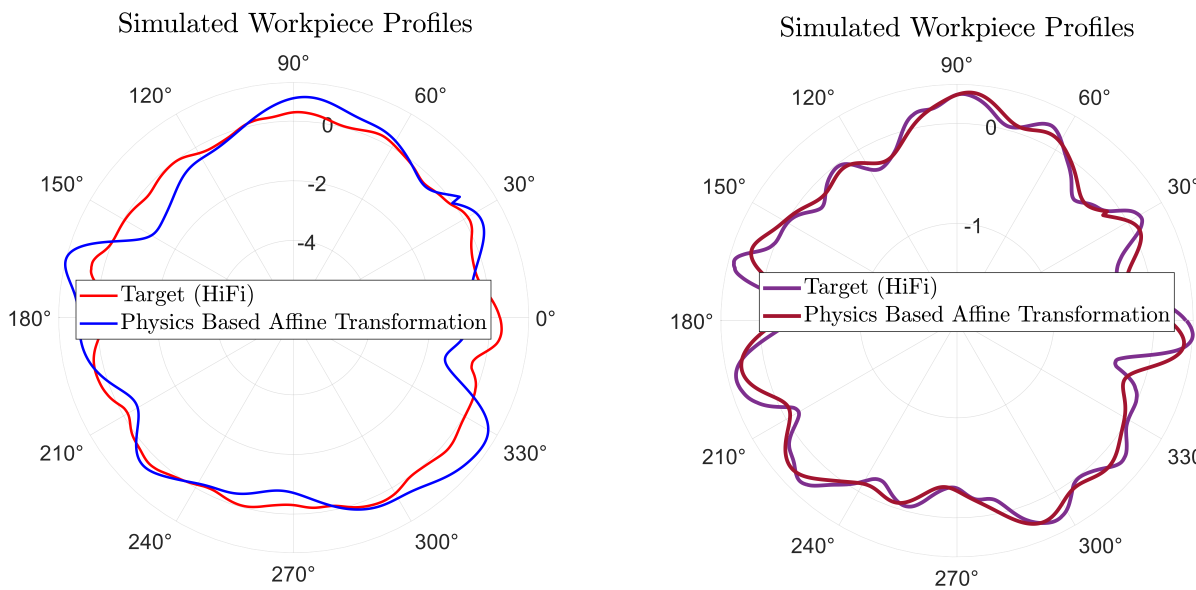


**Fig. 16.** Final profile prediction error. Target and predicted profiles of the training samples highlighted in Fig. 14 (a): the red one (on the left) and the violet one (on the right). (For interpretation of the references to colour in this figure legend, the reader is referred to the web version of this article.)

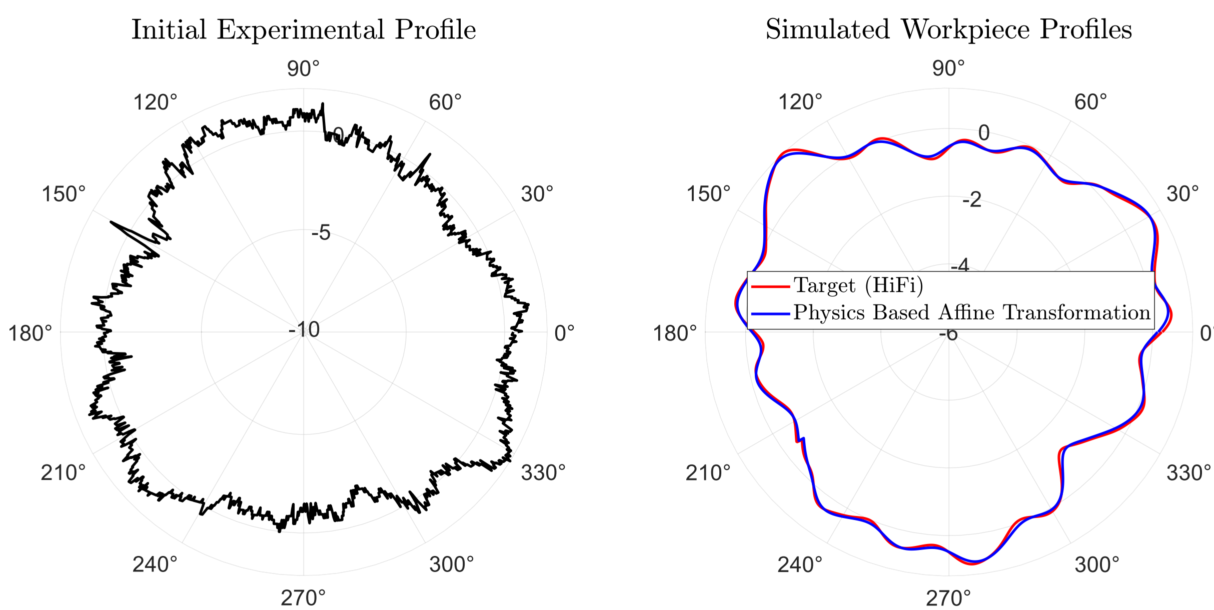


**Fig. 17.** Example of geometrical profile of a randomly selected test experiment, indicated as a red dot in Fig. 14 (b). Comparison with the static High-Fidelity model. (For interpretation of the references to colour in this figure legend, the reader is referred to the web version of this article.)

shrinking effect, which is chosen by minimizing the generalization error on the validation set in a classical dataset split.

It is worth noting that the penalty term of the regularization involves the transition matrix $\mathbf{G}_{dd}$ only, as the bias contribution is considered *a priori* important and decoupled with respect to the other components of the linear map. On the other side, the linear map predictors grow with $N_f^2$: therefore, depending on profile measurements sampling density, $\mathbf{G}_{dd}$ may become ill-conditioned due to predictors similarity and/or reduced number, and the corresponding identification sub-system needs to be regularized.

The optimization problem of Eq. (23) has a closed-form solution. In fact, by defining

$$\mathbf{D} := \begin{bmatrix} \mathbf{I}_{N_f \times N_f} & \mathbf{0}_{N_f \times 1} \\ \mathbf{0}_{1 \times N_f} & 0 \end{bmatrix} \in \mathbb{R}^{(N_f+1)\times(N_f+1)}$$

it yields

$$\widehat{\mathbf{T}}_{dd} = \mathbf{A}^T \left( \mathbf{A}\mathbf{A}^T + \eta \mathbf{D} \right)^{-1} \mathbf{O}$$

It has to be noted that, in usual centerless grinding production, WP profiles are measured by a roundness meter without a unique mechanical reference for the center and the angular position: the profile is numerically centred by a least square approach. While a roundness evaluation does not require the centre and angular references, the use of the initial and final profiles to train a DD model are impacted. The center position has an impact only on the one per turn component, but the error on the angular position has a generalized impact and must be limited by defining a unique mechanical reference for the angular position on each WP to be used when measuring the initial and final profiles.

Being the output multivariate (a vector), the general expression for prediction uncertainty is well represented by a covariance matrix.

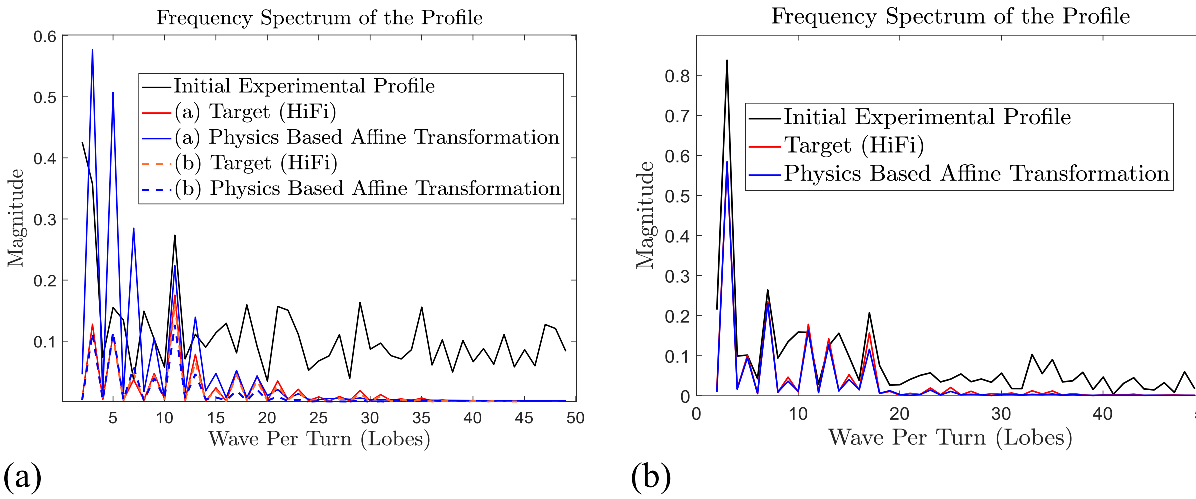


**Fig. 18.** FFT of the geometrical profiles: (a) the detachment samples shown by the violet and red dots in Fig. 16, and (b) a randomly selected test sample shown in Fig. 17. (For interpretation of the references to colour in this figure legend, the reader is referred to the web version of this article.)

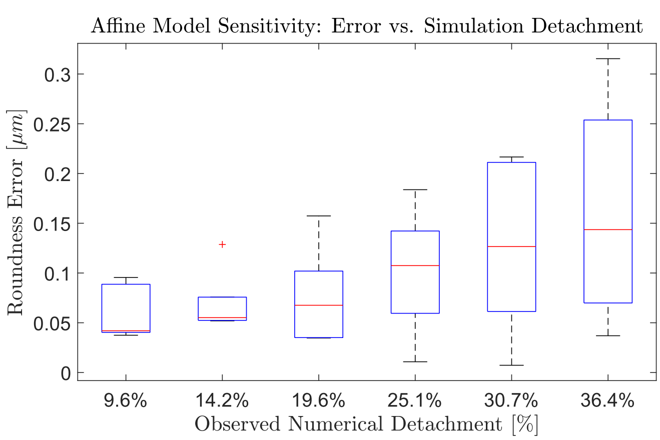


**Fig. 19.** Affine model sensitivity: error in the estimation of the final roundness as a function of the observed numerical detachment [%]

Assuming that the initial input profile is represented as a vector whose elements are i.i.d. and share the same variance $\sigma_{IN}^2$ (which can be traced back to the accuracy of the roundness measuring instrument used to acquire these profiles), it follows that:

$$Cov(\mathbf{o})_{ij} = \sigma_{IN}^2 \widehat{\mathbf{T}}_{dd} \widehat{\mathbf{T}}_{dd}^T + \mathrm{tr}\left(\sigma_{IN}^2 Cov\left(\widehat{\mathbf{T}}_{dd\ i,:}, \widehat{\mathbf{T}}_{dd\ j,:}\right)\right) =$$

$$= \sigma_{IN}^2 \left(\widehat{\mathbf{T}}_{dd} \widehat{\mathbf{T}}_{dd}^T + \mathrm{tr}\left(Cov\left(\widehat{\mathbf{T}}_{dd\ i,:}, \widehat{\mathbf{T}}_{dd\ j,:}\right)\right)\right)$$

where

$$Cov\left(\widehat{\mathbf{T}}_{dd\ i,:}, \widehat{\mathbf{T}}_{dd\ j,:}\right) = \sigma_E^2 \left(\mathbf{A}\mathbf{A}^T\right)^{-1}$$

and $\sigma_E^2$ is the unknown residuals variance that can be approximated by the following unbiased estimator:

$$\sigma_E^2 = \frac{\left\|\mathbf{O} - \widehat{\mathbf{T}}_{dd}\mathbf{A}\right\|_F^2}{N_e - N_f}$$

where $\|\ldots\|_F$ indicates the Frobenius norm.

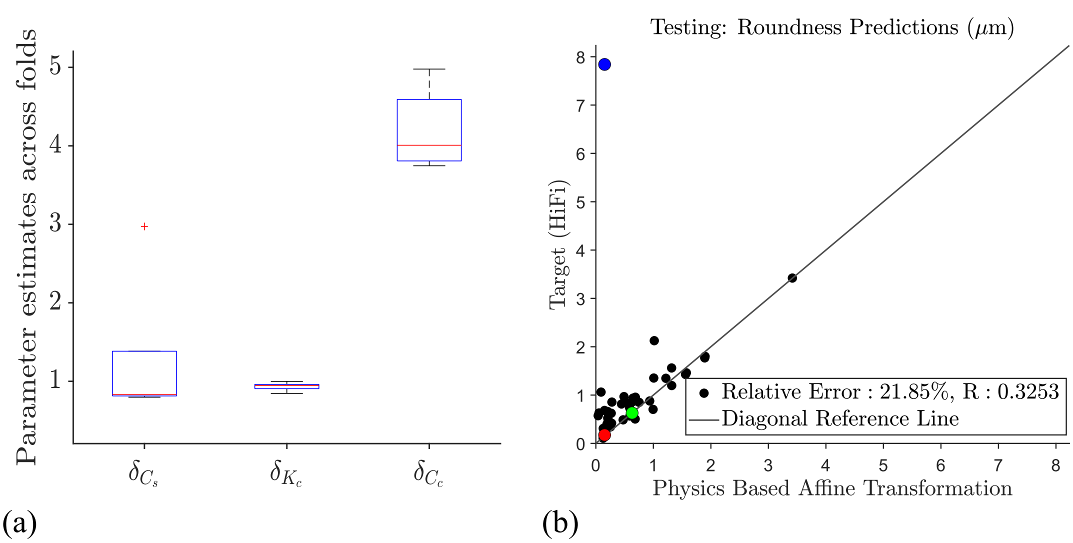


**Fig. 20.** (a): Distribution of model correction parameter estimates across folds; (b): Roundness predictions for Fold 4 of the *K*-fold cross-validation testing phase. The experiments corresponding to blue (A), red (B) and green (C) dots are investigated in the following.

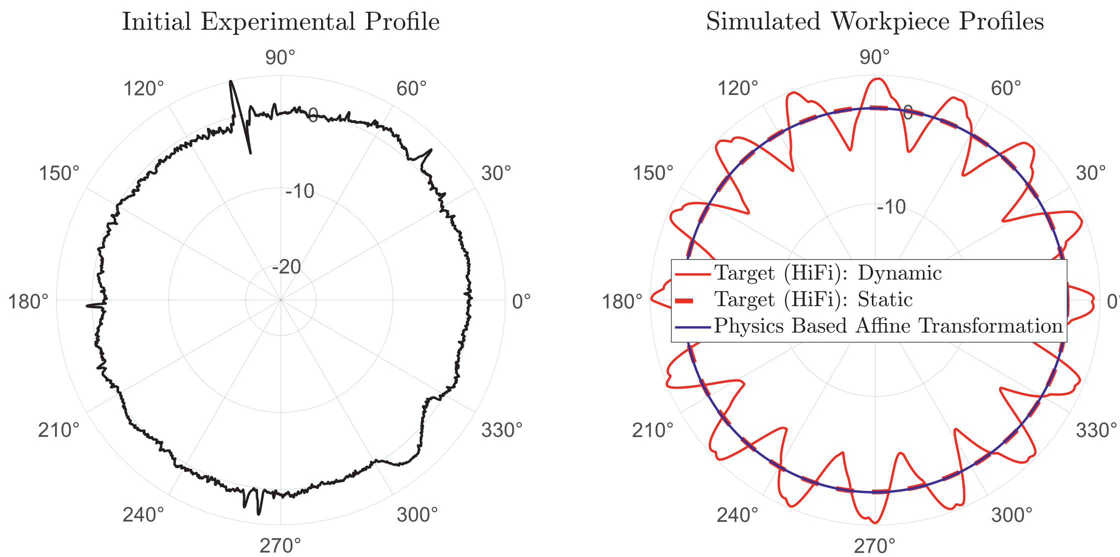


**Fig. 21.** (a) Example of geometrical profile of a maximum error selected test experiment, indicated as a blue dot in Fig. 20 (b). (For interpretation of the references to colour in this figure legend, the reader is referred to the web version of this article.)

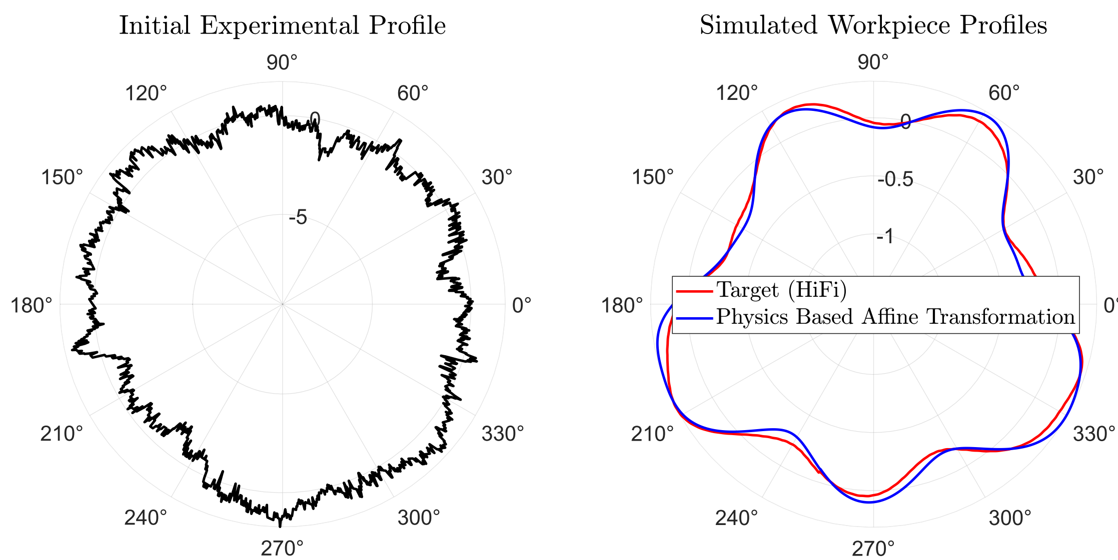


**Fig. 22.** Example of geometrical profile of the min error test experiment (C), indicated as a green dot in Fig. 20 (b). Plot (a): initial profile; plots (b) final profiles predicted by the dynamic High-Fidelity model and the static physics-based affine transformation. (For interpretation of the references to colour in this figure legend, the reader is referred to the web version of this article.)

## 6. Models validation

### 6.1. Design of virtual experiments using a high-fidelity ground truth model

In order to test the proposed approaches in a controlled environment, a set of virtual experiments were conducted using a HiFi dynamic simulation model as the reference or "ground truth". Indeed, within the proposed framework, the primary requirement is not an exact match with real-world measurements, but the availability of realistic simulated data in which the initial and final WP profiles are coherently and consistently correlated. The adoption of the HiFi model allows full control of the process conditions, enabling the evaluation of specific phenomena on model performance (see, for example, the analyses in 6.2.2 and 6.2.3). In the model, inspired by [19], the material removal is computed by considering the intersection between the WP (modelled as a radial *z-buffer*) and an ideal circular operating wheel. Two versions of the model have been developed. The first (denoted as *static*) neglects the relative machine–WP dynamics and considers only the static compliance, including the wheel–WP contact stiffness. The second version (denoted as *dynamic*) incorporates the relative wheel–WP dynamics, described by a vector of modal parameters. The equilibrium under the grinding forces is computed using a fixed-step Newmark integration scheme with error monitoring. In the models validation section, this dynamic formulation is employed to validate the DD affine transformation learned from datasets of raw and final profiles, showing how such a transformation has sufficient expressive power to capture the underlying dynamic behaviour as well. Differently from [19], our HiFi model considers both volumetric and edge components of the grinding force.

The dynamic HiFi model relies on a set of intrinsic system parameters that define the machine–WP dynamics. These include the mass and stiffness of the machine structure, damping characteristics, cutting stiffness, and energy-related parameters such as the volumetric specific energy and edge component. The HiFi model does not explicitly account

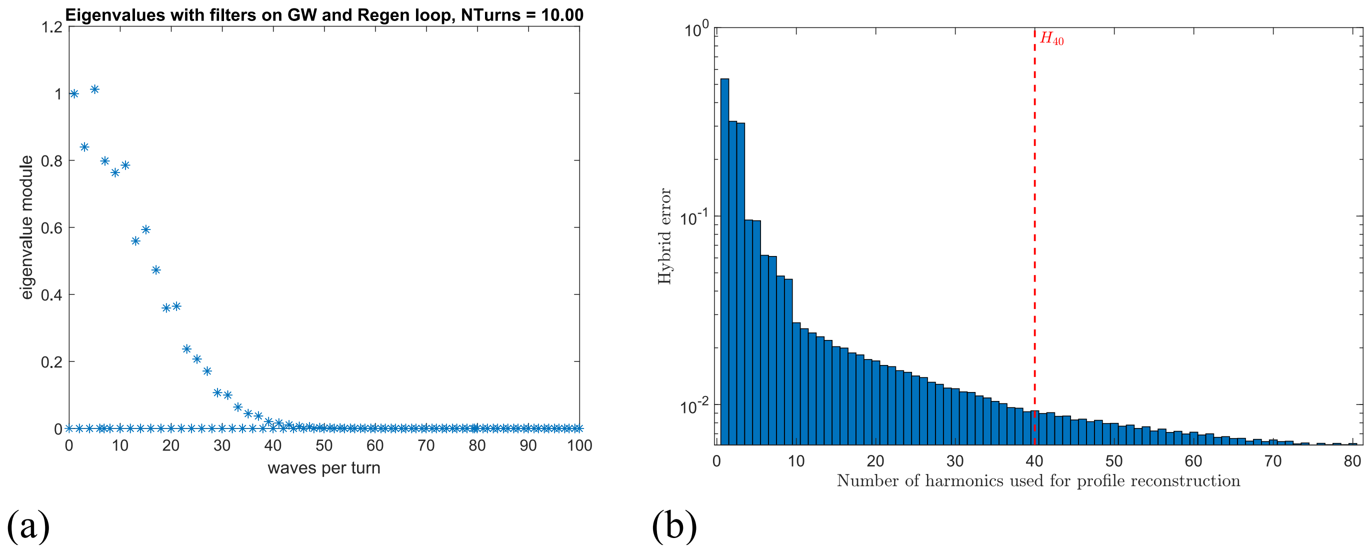


**Fig. 23.** (a): Eigenvalues of the physics-based transformation matrix for the process in Table 1; (b): Error in the calculation of the final profile roundness, considering only a limited number of harmonics.

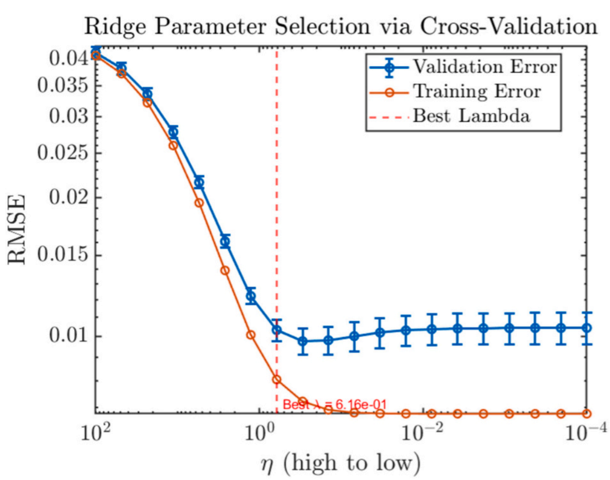


**Fig. 24.** Cross-validation results used to identify the optimal regularization parameter η for the ridge regression-based data-driven affine transformation model.

for parameters such as the mechanical properties of the WP material and the grinding wheel: their influence is captured indirectly through variations in grinding stiffness, contact stiffness, and specific energy. Together, these parameters control the system's dynamic response and influence critical variables, including the stiffness factor and contact length. The parameters used in the dynamic HiFi simulations are summarized in Table 2.

A factorial Design of Experiments (DoE) was adopted to systematically investigate the influence of key process parameters on the manufacturing process. The HiFi model accurately simulates the detailed physics and complex interactions of the process under varying operating conditions. Table 3 reports the control parameters varied in the DoE, together with their ranges and levels, while Table 4 summarizes the fixed parameters that were held constant. A reduced set of 210 experiments was generated using Latin Hypercube Sampling (LHS) to serve as a benchmark for validating the proposed PB affine transformation model.

The HiFi process model has previously been validated on a reduced set of grinding experiments, demonstrating its suitability for providing realistic profiles [26]. As an example, a couple of comparisons between predicted and experimental profiles are shown in Fig. 12.

### 6.2. *Validation of physics-based affine transformation model*

#### 6.2.1. *Validation under static operating conditions*

In this section, the PB affine transformation model is validated against the outputs of the *static* HiFi model on the virtual experimental dataset, described in Section 6.1, to assess the accuracy of the proposed approach in reproducing the complex dynamics simulated by the HiFi model.

A *K-fold* Cross-Validation (CV) was used to evaluate generalization performance. In this study, the dataset was randomly partitioned into $K = 5$ mutually exclusive folds of approximately equal size. In each iteration, $K$-1 folds were used for training and the remaining fold was used for testing. During training, the nominal parameters of $C_{s0}$, $C_{c0}$ and $K_{c0}$ [4], as described in Section 3, were corrected using factors $\delta_{C_s}, \delta_{C_c}, \delta_{K_c}$, estimated by minimizing the multi-target loss function of Eq. (8) on the training folds. This process was repeated $K$ times so that each fold was used as the test set exactly once.

The geometrical profiles from the HiFi model and affine models were compared, quantifying the similarity by the HybErr and the linear correlation coefficient between the roundness and the MEHE on the profile spectra. Both HybErr and MEHE were computed with a smooth factor of 0.5 µm. The correction factors identified by the calibration procedure are reported in Table 5.

Then, the calibrated model was tested on unseen process conditions to evaluate its generalization capability. Fig. 13 (a) shows the boxplot of parameter estimates across all folds, illustrating their distribution. Performance metrics from each iteration were aggregated using a weighted average (see the top legend in Fig. 13 (b)), accounting for differences in fold sizes.

To further illustrate the predictive performance of the model, the scatter plot of Fig. 14 compares all roundness predictions with the corresponding targets for both the training and testing datasets. Most points show strong agreement between the HiFi and PB affine transformation model, as quantified by the linear correlation coefficient (R) and the average HybErr.

A few points substantially deviate from the diagonal line. A plausible reason for these deviations can be traced back to the detachment at the beginning of the process, that is correctly represented by the sole ground truth model (HiFi), while it produces a non-physical negative material removal in the linear affine model. This typically occurs in particular

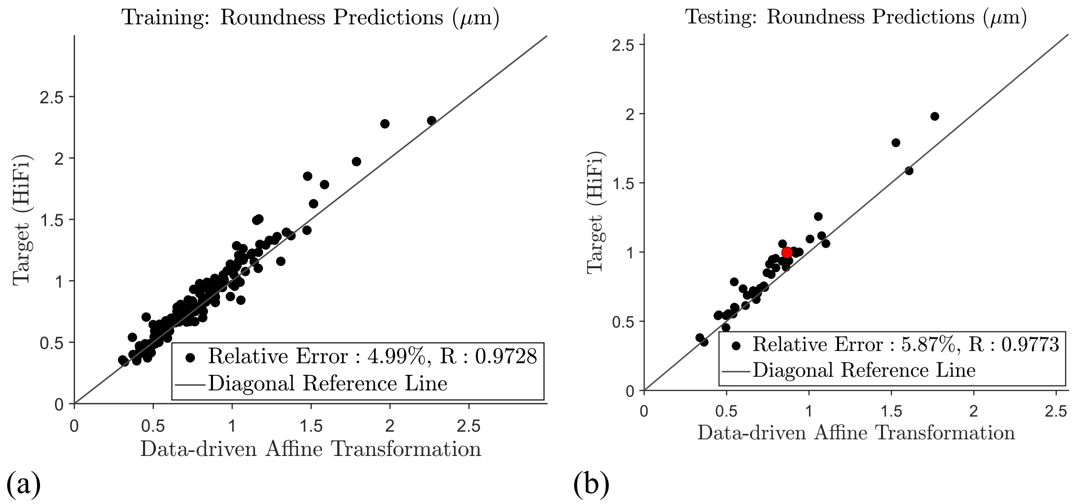


**Fig. 25.** Roundness comparison between High-Fidelity targets and the data-driven affine transformation predictions for (a) training and (b) testing sets. The test indicated by the red dot is described in Fig. 27. (For interpretation of the references to colour in this figure legend, the reader is referred to the web version of this article.)

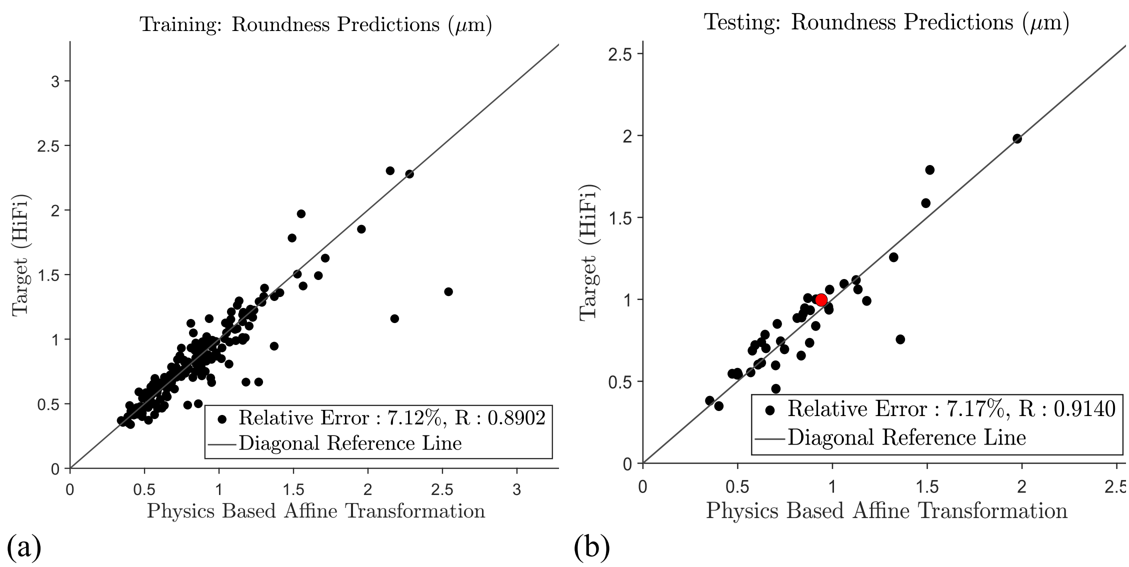


**Fig. 26.** Roundness comparison between High-Fidelity targets and the physics-based model calibrated on the fixed process dataset: predictions for (a) training phase and (b) testing sets (to be compared to the data-driven results, as shown in Fig. 25). The test indicated by the red dot is described in Fig. 27. (For interpretation of the references to colour in this figure legend, the reader is referred to the web version of this article.)

cases, e.g., when the initial profile is characterized by a strong localized peak (as exemplified by the peculiar profile of Fig. 15 (a)). The corresponding operation sample, associated with poor model performance (see the red dot in Fig. 14 (a)), exhibits a relevant initial detachment, which can be appreciated by observing the Material Removal Rate (MRR) behaviour, provided by the HiFi model, in Fig. 15 (b), represented by the red line (the detachment zone is boxed in black). Conversely, an operation sample characterized by a good performance, such as that corresponding to the violet dot in Fig. 14 (a), does not exhibit any significant initial detachment (Fig. 15 (b), violet line). A comparison in terms of profile error is provided in Fig. 16. The effect of detachment is further analysed in the following Section 6.2.2.

To provide a general idea of model quality, an experiment was randomly selected from the test dataset, with the process parameters listed in Table 6. The close match between the predicted and HiFi profiles shown in Fig. 17 confirms that the affine model can reproduce the detailed geometrical features across variable process conditions.

Finally, the frequency-domain characteristics of the same profiles were examined. The Fig. 18 presents the corresponding FFTs: (a) shows the FFT of the red-dot and violet-dot samples of Fig. 14 (roundness measurements) and Fig. 15 (corresponding MRR). The overall comparison between the ground truth (HiFi) and the PB affine transformation yielded a MEHE of average 0.091 $\pm$ 0.115 for training and 0.085 $\pm$ 0.084 for testing, showing that the predicted profiles accurately preserve the spectral content of the HiFi static model.

To further evaluate the effectiveness of the adopted affine transformation, the final profiles have been estimated also by the traditional approach that assumes an independent evolution of each harmonic profile component, i.e., forcing to zero all elements of the transformation matrix outside the main diagonal. The resulting errors in final roundness estimation become 26.6% during training and 25.8% for testing; almost three times the errors of the PB affine transformation. This confirms the importance of reproducing the interaction between different harmonic contents, as done by the PB affine transformation.

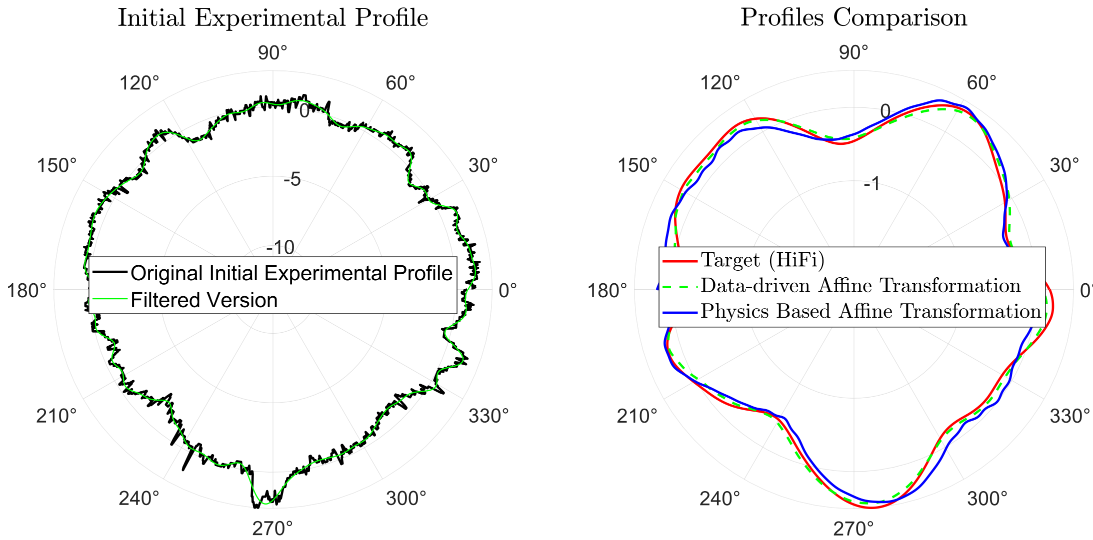


**Fig. 27.** Comparison of predicted profiles starting from the same initial profile: data-driven and physics-based affine models vs High-Fidelity target (referred to the red dot sample, see Fig. 25-b and Fig. 26-b). (For interpretation of the references to colour in this figure legend, the reader is referred to the web version of this article.)

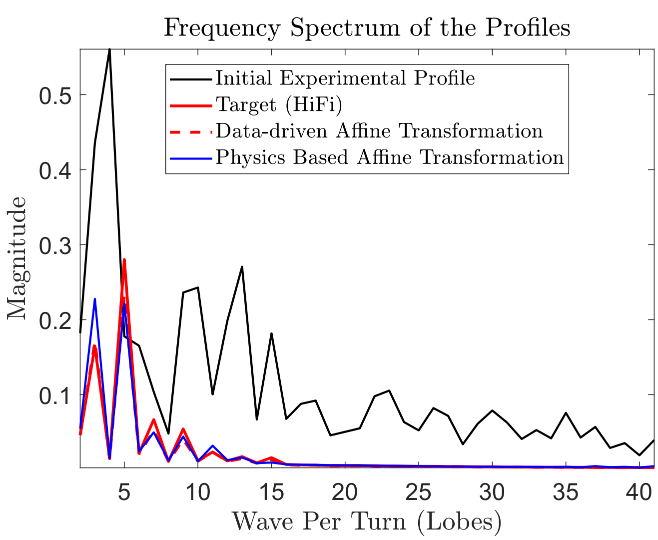


**Fig. 28.** FFT comparison for the randomly selected sample shown in Fig. 27.

#### 6.2.2. Model sensitivity to contact detachment

To better understand the impact of the detachment phenomenon on the proposed PB affine transformation, a virtual DoE has been executed, exploiting the flexibility of the HiFi model. Different levels of detachment have been obtained considering five distinct profiles, with initial roundness ranging from 3.50 to 9.35 μm, and artificially increasing their initial waviness by multiplying them by a scale factor ranging from 0.75 to 2.0 in steps of 0.25. The resulting set of 30 experiments has been processed by the HiFi model and by the PB affine transformation (correction factors listed in Table 5). The analysis has been performed on the process described in Table 1, with a feed per turn of $f_z = 3\ \mu$m.

The resulting errors in roundness estimation are documented in Fig. 19, as a function of observed numerical detachment (i.e., percentage of time samples where detachment occurs, provided by the HiFi model).

The results indicate that the median roundness error remains remarkably stable at lower detachment levels, with a narrow distribution and a median below 0.05 μm at 9.6% detachment. However, beyond 25.1% the interquartile range expands and maximum residuals approach 0.32 μm, signalling a degradation in model robustness. Nevertheless, the linear model performs well even at high levels of initial detachment, maintaining a median error below 0.15 μm even at 36.4% detachment.

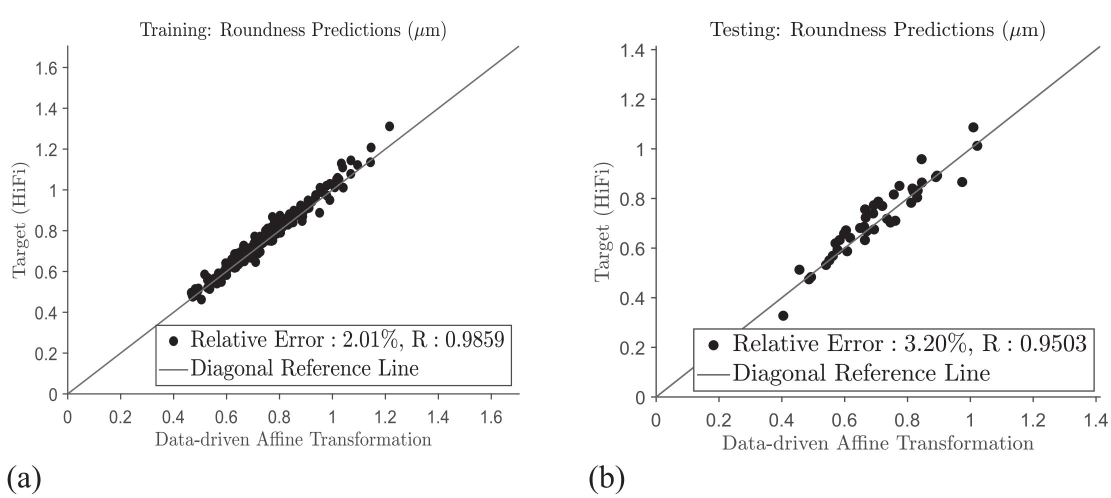


**Fig. 29.** Roundness comparison between High-Fidelity targets and the data-driven affine transformation predictions for (a) training and (b) testing sets.

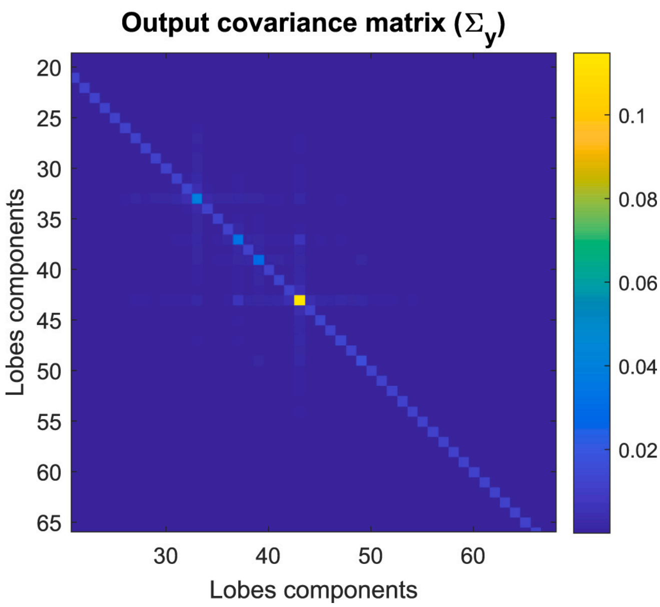


**Fig. 30.** Covariance matrix of the predicted profile.

**Table 2**
Summarizes the intrinsic High-Fidelity model parameters used in the simulations.

| Parameter | Symbol | Value | Unit |
|---|---|---|---|
| Mass | $M_q$ | 995 | Kg |
| Relative Machine Stiffness | $K_q$ | 146,570 | N/mm |
| Damping ratio | ζ | 0.05444 | |
| Contact Stiffness | $K_c$ | 24,802 | N/mm |
| Volumetric Specific energy per unit length | $E_v$ | 282.8666 | $\frac{N}{mm^2}$*s |
| Edge Component | $E_e$ | 0 | N/mm |

**Table 3**
Control parameters in virtual experiments for validation.

| Control Parameters | Range | Unit | Levels |
|---|---|---|---|
| $h_{w_i}$ | 3 - 18 | mm | [3,8,18] |
| $f_{z_i}$ | 20 - 150 | µm | [20,80,100,150] |
| $\Omega_{CW}$ | 8 - 20 | rpm | [8,15,20] |
| $\gamma_i$ | 30, 20 | ° | [20,30] |
| $N_{r_i}$ | 8 - 15 | - | [8,10,15] |
| $N_{r_{spark-out}}$ | 0.7 - 5.7 | - | [0.7, 1.6, 2.5, 4.1, 5.7] |
| $d_{w_i}$ | 16 - 36 | mm | [16,36] |

**Table 4**
Fixed process parameters used in virtual experiments.

| Fixed Parameters | Range | Unit |
|---|---|---|
| $d_s$ | 610 | mm |
| $\Omega_S$ | 1000 | rpm |
| $d_{CW}$ | 355 | mm |
| WP material | C45 | – |
| $b$ | 146 | Mm |

It must also be considered that, in industrial applications, rougher initial WPs require longer processes to reach an adequate finishing level. Therefore, even if detachment occurs in the initial process phase, the relative importance of detachment does not increase. This systematically limits the importance of the detachment, reducing the error associated with the affine approximation.

**Table 5**
Estimated correction factors for the physics-based affine transformation model.

| Parameter | Correction Factor ($\delta$) |
|---|---|
| $C_{s0}$ | 0.7165 |
| $C_{c0}$ | 0.9401 |
| $K_{c0}$ | 0.9672 |

**Table 6**
Process parameters of a randomly selected sample.

| Parameter | Value | Unit |
|---|---|---|
| $h_w$ | 3 | mm |
| $f_z$ | 8 | µm |
| $\gamma$ | 30 | ° |
| $d_w$ | 36 | mm |
| $d_s$ | 610 | mm |
| $d_{cw}$ | 355 | mm |
| $\Omega_{WP}$ | 1.3148 | rps |
| $N_r$ | 8 | – |
| $N_{r_{spark-out}}$ | 1.6 | – |
| $M$ | 1800 | |

### 6.2.3. *Model performance under dynamic operating conditions*

In this section, the performance of the proposed PB affine transformation model is assessed using the outputs of the *dynamic* version of the reference HiFi model, that reproduces the WP-machine dynamics, with the parameters reported in Table 2. The objective is to evaluate the limits of the static version of the affine transformation, proposed in this study.

The virtual experimental dataset described in Section 6.1 was employed, covering a wide range of process conditions to ensure variability in both excitation sources and system responses. The analysis methodology, in terms of error definition, model optimization, and cross fold validation, was the same as that of the static validation documented in Section 6.2.1.

The distribution of the correction factors identified during the calibration procedure across the CV folds is presented in Fig. 20 (a). The identified correction coefficients $\delta_{C_s}$ and $\delta_{Kc}$ are near to 1, similarly to the comparison with the static reference model. The contact length with the control wheel, tuned by $\delta_{C_c}$, is significantly increased by the optimization. This is due to the fact that the static PB affine model is trying to (partially) emulate the frequency response of the structural dynamics by the contact filter, that acts in series with the contact filters. Those filters, nevertheless, cannot reproduce the low damping peak of the mechanical structure: this generates a higher error in the roundness estimation. The average HybErr on the roundness was 0.243 ± 0.005 µm for the training set and 0.25 ± 0.02 mm for the test set. Regarding spectral accuracy, the MEHE was 0.17 ± 0.06 µm for the training set and 0.18 ± 0.07 µm for the test set.

The correction factors from Fold 4 were selected by minimizing the CV loss. For this specific fold, the training phase achieved a HybErr of 24.94%, $R = 0.58$ and an MEHE of 0.1784 ± 0.1436 µm. The corresponding testing phase yielded a HybErr of 21.85%, $R = 0.32$ (see Fig. 20 (b)) and an MEHE of 0.1612 ± 0.1368.

To investigate the impact of system dynamics on the model's predictive accuracy, a detailed comparison was performed for the samples highlighted in Fig. 20 (b). The corresponding process parameters are reported in Table 7. Sample A corresponds to the blue dot (maximum-error case), while Sample B corresponds to the green dot (minimum-error case). Fig. 21, Fig. 22 illustrates the resulting geometrical profiles.

The left plot in Fig. 21 (a) represents the experimentally measured initial profile, while the right plot (b) shows the target (HiFi, *dynamic*) geometrical profile, which exhibits a large waviness at 16 lobes.

**Table 7**
Process parameters of the samples highlighted in Fig. 20 (b).

| Parameter | Sample A (max error) | Sample B (min error) | Unit |
|---|---|---|---|
| $h_w$ | 18 | 3 | mm |
| $f_z$ | 15 | 2 | μm |
| $\gamma$ | 20 | 30 | ° |
| $d_w$ | 16 | 36 | mm |
| $d_s$ | 610 | 610 | mm |
| $d_{cw}$ | 355 | 355 | mm |
| $\Omega_{WP}$ | 5.55 | 2.47 | rps |
| $N_r$ | 9 | 14 | – |
| $N_{r_{spark-out}}$ | 2.5 | 5.7 | – |
| $M$ | 1800 | 1800 | |

Considering the WP angular speed ($\Omega_{WP}$= 5.54 rps, see Table 7), the waviness corresponds to oscillations near 89 Hz. While the structural parameters reported in Table 2 produce an open loop resonance near 61 Hz, oscillations at a higher frequency are expected when the structural loop is closed by the grinding process. To investigate the relevance of the dynamic response, the capabilities of the HiFi models have been exploited, repeating the experiment with the static HiFi model (experiment C). The dashed red line in Fig. 21 (b) shows the final profile produced by the static HiFi model, confirming that the process instability at 16 lobes per turn was related to the structural dynamics and that the PB affine model is coherent with the forecasting produced by the static HiFi model (red dot in Fig. 21 (b)), as already discussed in 6.2.1. The comparison with the static HiFi model is represented by the red dot in Fig. 20 (b).

In contrast, other experiments performed with the dynamic HiFi model show that the PB static affine transformation performs well when the process does not excite the structural resonances. For example, the outcome of experiment (C), represented by the green dot in Fig. 20 (b), is described in Fig. 22. In this case, the profile evolution is dominated by the initial geometry and steady-state kinematics. The PB affine model achieves a near-perfect match with the reference model, confirming its reliability for the majority of stable operating conditions.

### 6.3. *Validation of the data-driven affine transformation in frequency domain*

This section presents the validation of the DD approach for identifying the affine transformation between the initial and final geometrical profiles, provided by the ground truth (HiFi) simulations described in the previous section. The analysis is carried out under the fixed process conditions listed in Table 1 and relies on the first (*static*) version of the HiFi model.

An efficient model identification requires reducing the number of features used to describe the initial and final WP profiles. Given the analysis developed in Section 4.3, a truncation in the frequency domain is adopted focusing on the low order harmonic waviness that grows in case of rounding instability, with a limited error on the preserved harmonic components. This approach is also of interest because it nicely agrees with the usual reasoning done by domain experts in terms of stable and unstable lobe orders.

Fig. 23 (a) represents, on the left, the lower frequency eigenvalues of the transformation matrix for the process conditions of Table 1. Given the 10 turns duration of the process, which is stable, the modulus of the eigenvalues is strongly reduced, compared to the typical values for the one step transformation matrix (see, for example, the eigenvalues plotted in Fig. 10), because of the contact filters effect. As a consequence, in the final WP profile the contribution of the higher frequency harmonics is negligible. Fig. 23 (b) shows the error in computing the roundness on the final profile as a function of the number of preserved harmonics. Analysing those plots, it has been decided to truncate the model to the first 40 harmonics, with a 0.9% HybErr on the final roundness, to identify the DD model.

The affine transformation was learned using the ridge regression-based method described in Section 5. The regularization parameter ($\eta$) was set at 0.62 by CV, as shown in Fig. 24, balancing model complexity and the generalization error. The validation was performed as for the PB model in Section 6.2, computing the MEHE spectral error and the HybErr on the roundness with respect to the profiles produced by the HiFi model. The roundness error is evaluated after transforming back to the spatial domain the predicted frequency-domain output. Fig. 25 compares the roundness values between the DD and HiFi models, for both training and testing sets.

Furthermore, to compare DD and PB model performance focusing on a specific process condition, also the PB model has been calibrated on the fixed process dataset of Table 1. In this case, the errors of the PB model decrease, with respect to those of Fig. 14, respectively to 7.17% for the roundness measurement and to a MEHE of 0.0657 $\pm$ 0.0476 for the spectra. The scatter plots in Fig. 26 present the overall accuracy analysis, to be compared to the corresponding DD accuracy in Fig. 25. These results confirm that the PB affine transformation, when adjusted with the identified correction factors, can reliably reproduce the static HiFi model roundness, even if with a lower accuracy compared to the corresponding DD model. A few points deviate from this linear trend, due to the detachment instances, which were discussed in Section 6.2 (see Fig. 15).

To provide further support to model validity, Fig. 27. presents a randomly selected sample (the red dot in Fig. 25-b and Fig. 26-b) from the test dataset of the DD model identification. The figure shows on the left the original initial profile and the filtered version, obtained considering only the harmonic terms preserved in the frequency domain. On the right, the (HiFi) target profile is compared to the profiles produced by the DD and the PB affine transformations. While both models provide a good estimate of the final profile, the DD model appears, also visually, to be more accurate than the PB model.

Fig. 28 presents the FFT of the same sample. The spectral content closely matches the HiFi target, DD and PB model spectra, confirming that both models accurately capture the frequency characteristics of the process.

The overall spectral error metrics were also evaluated on all experiments: the average MEHE is 0.041 $\pm$ 0.028 for training and 0.052 $\pm$ 0.030 for testing, confirming consistent performance of the DD affine model.

#### 6.3.1. *Validation under dynamic operating conditions*

After validation under *static* conditions, the analysis is extended to the *dynamic* version of the HiFi model, to evaluate the capability of the DD affine transformation to capture the effects of machine–WP dynamics. The same training and testing datasets used in Section 6.3 are considered, ensuring a consistent validation framework.

Expecting the presence of higher order waviness produced by the structural resonance, the selection of the required number of harmonics is repeated for the experiments produced by the dynamic model. In this case, the number of retained harmonics for the DD model is increased to 70, resulting in a 0.3% HybErr on the final roundness for the truncated representation.

The DD model is then identified following the same ridge regression-based procedure described in Section 5, including the estimation of the regularization parameter ($\eta$), set to 0.0695 by minimizing the *5-fold* CV loss on the training set. As previously described, the validation is performed after transforming the predicted frequency-domain output back into the spatial domain and computing the corresponding roundness values.

Fig. 29 (a) and (b) show the comparison between the roundness values obtained from the dynamic HiFi simulations and those predicted by the DD model for the training and testing datasets, respectively.

The results demonstrate that the DD model captures the influence of structural dynamics on the final WP profile. In comparison with the static PB affine transformation, the DD model exhibits significantly improved predictive capability, as it inherently learns these effects from the training data.

In addition to the roundness-based validation, the spectral accuracy of the DD model under dynamic conditions is evaluated through the MEHE, computed between the DD predictions and the target (HiFi, *dynamic*) frequency-domain representations. The obtained results show an average MEHE of $0.013 \pm 0.071$ for the training set and $0.021 \pm 0.010$ for the testing set. These values are consistent with those observed under static conditions and confirm that the DD affine transformation accurately reproduces not only the overall roundness but also the detailed spectral content of the profiles, including the higher-order harmonics induced by the structural resonance.

As discussed in Section 5, the model accuracy can be evaluated by computing the covariance matrix of the predicted profiles. This is obtained from the estimated residual variance and the variance of the input, the latter assumed to coincide with the measurement accuracy of the roundness instrument used to acquire the profiles [33] (0.2 μm in the present case).

The resulting covariance matrix (Fig. 30) is nearly diagonal, indicating that the waviness components are only marginally correlated. A higher variance is observed for component #43, related to the higher gain shown by the HiFi model for that harmonic.

These results demonstrate that the DD affine transformation accurately maps initial to final profiles in both spatial and frequency domains, under static and dynamic conditions. In comparison, the accuracy of the PB model is only marginally improved when the correction factors are calibrated for the specific process conditions, and only in the static case (see Fig. 26). It can also be observed that the measurement noise associated with instruments commonly used to assess WP profiles is negligible when compared to both the model generalization error and the specified accuracy requirements [33].

## 7. Conclusions

Centreless grinding is a widely used machining process for cylindrical mechanical parts in different industries, such as automotive and aerospace, due to its accuracy, productivity and versatility in terms of process parameters, workpiece (WP) materials and sizes. Of particular importance is therefore a detailed understanding of the relationship between the input conditions, including the initial WP profile, and the process capability to meet the specified geometric tolerance specifications, such as WP roundness on the final WP profile. While several studies have been performed focusing on the evaluation of process stability in the time or frequency domain, this paper analyses an original approach (partially introduced by the authors in [16]), where the process is represented by an affine transformation that directly links the initial and final profiles.

The proposed approach has been validated using a High-Fidelity (HiFi) process model, which served as the ground truth, allowing full control of the involved phenomena. The general characteristics of the profile transformation have been studied: given that the transformation is represented by a companion matrix, it has been demonstrated that the eigenvectors are quasi-harmonic functions along the WP profile. As a consequence, the transformation matrix in the frequency domain is almost a diagonal matrix, with limited coupling between different harmonic terms. This allows consideration of the absolute value of the transition matrix eigenvalues, referred to the number of waves in the corresponding eigenvector, to get an informative overall description of the process dynamics, analogously to a frequency response function for dynamical systems in the time-domain. The affine transformation correctly reproduces the marginal but not negligible interdependencies between different harmonic components: the approximation of assuming that each harmonic depends only on the corresponding term in the input profile, as often done in industrial practice, has been evaluated. The HiFi model allowed the execution of virtual experiments to separately quantify the effect of phenomena not included in the Physics-Based (PB) affine transformation, like grinding wheel-workpiece detachment and structural machine dynamics.

Furthermore, the direct profile transformation approach allowed the development of an original non-parametric, Data-Driven (DD) affine process model in the waves-per-turn domain. It allows a rapid model identification based only on the measurement of the initial and final WP profiles, easily done also in an industrial environment. Once identified, the DD model, that effectively reproduces also the structural dynamics effects, can be exploited to evaluate how a new batch of raw WPs (with known profile characteristics) influences the final WP roundness.

With the proposed approach, the process models can be exploited to simultaneously optimize the roughing and finishing phases, investigating how they attenuate the different waviness components, as discussed in [16]. Differently from the asymptotic approach of stability analyses typically proposed in the literature, the transformations correctly consider the finite duration of each phase. Overall, the present work fits within the broader research line, in the grinding field, aimed at identifying process conditions that ensure the acceptability of the final product [34].

The procedure proposed to identify DD models (i.e., measurement of the initial and final profiles, with appropriate phasing, order reduction in the waves-per-turn domain) will be exploited, in a future development, to generalize the current linear DD model, limited to operations with fixed process parameters (e.g., feed per turn, WP height, and number of WP turns), in order to handle variable operating conditions. Nonlinear machine learning approaches, such as artificial neural networks, will be evaluated.

Future work will extend the proposed PB transformation, augmenting the current static modelling framework to incorporate machine's and wheels dynamic response into the affine transformation, which has been shown to have, in some cases, a relevant effect on regenerative chatter onset. Both PB and DD approaches will be applied to WP profiles gathered during experimental campaigns, to further validate and refine the proposed methodology.

## CRediT authorship contribution statement

**Lohit Kumar Pentakota:** Writing – original draft, Validation, Software, Methodology, Investigation, Data curation, Conceptualization. **Marco Leonesio:** Writing – original draft, Methodology, Investigation, Funding acquisition, Formal analysis, Conceptualization. **Moschos Papananias:** Writing – review & editing, Investigation, Formal analysis. **Giacomo Bianchi:** Writing – original draft, Supervision, Methodology, Investigation, Funding acquisition, Formal analysis, Conceptualization.

## Declaration of competing interest

The authors declare that they have no known competing financial interests or personal relationships that could have appeared to influence the work reported in this paper.

## Acknowledgements

The authors gratefully acknowledge Claudia Ceresa and Alessandra Tafaro for their technical and administrative support in STIIMA-CNR. They also express their gratitude to the PhD program of National Interest in Robotics and Intelligent Machines (DRIM), for providing the scientific framework for this research, and to Monzesi S.p.A. for providing industrial support.

## Appendix A. : Existence of a marginally stable 1 per turn component

The WP profile is described by the radial distance from a reference circumference with an arbitrary diameter and center (see Fig. 6). Moreover, the conventional kinematic process model (as detailed in [1]) is linear and assumes that the profile is almost circular (i.e., the roundness error is small, compared to the mean radius): for this reason the center of the mean, best fit circumference is adopted. This corresponds, from the experimental point of view, to the fact that the WP is placed on the roundness meter without exploiting a mechanical centering feature: the center is defined in order to minimize the mean square radial error. As the specific choice of the reference center is arbitrary, it must have no effect on process simulation and on the estimated final profile. From the mathematical point of view, the transition matrix **G** must have at least one marginally stable eigenvalue (i.e., indifferent equilibrium), associated with a sinusoidal eigenvector with periodicity of 1-per-turn, which is moreover orthogonal to the other eigenvectors.

In fact, when the offset $\overrightarrow{\boldsymbol{o}}$ of the reference origin from the mean circumference is small, compared to the mean radius, the eccentricity adds to the WP profile a one per turn harmonic term:

$$\boldsymbol{e}_1 := [|\overrightarrow{\boldsymbol{o}}| \sin(i\Delta\theta + \varphi)]^T := [\mathrm{a}\sin(i\Delta\theta) + b\cos(i\Delta\theta)]^T, \; i = 1, 2, \ldots, N_d$$

where $|\overrightarrow{\boldsymbol{o}}| := \sqrt{a^2 + b^2}$ and $\tan\angle\overrightarrow{\boldsymbol{o}} := a/b$. Then, given the linear nature of the affine transformation, we can analyse how the process acts on $\boldsymbol{e}_1$. The first row of the **G** matrix provides the updated cumulated material removal produced by the grinding operation, neglecting here, for simplicity, the contact filters, given that their effect is negligible at the one per turn frequency. Now, consider the discretized notable angles $\alpha_d$ and $\beta_d$ defined in Eq. (10); the aforementioned material removal is given by

$$\begin{aligned}
\boldsymbol{e}_2^{(1)} &= [g_{1i}]\boldsymbol{e}_1 = kK_1(a\sin\alpha_d + b\cos\alpha_d) - kK_2(a\sin(\pi - \beta_d) + b\cos(\pi - \beta_d)) + (a\sin 0 + b\cos 0)(1-k) \\
&= k\frac{\sin\beta_d}{\sin(\beta_d + \alpha_d)}(a\sin\alpha_d + b\cos\alpha_d) - k\frac{\sin\alpha_d}{\sin(\beta_d + \alpha_d)}(a\sin\beta_d - b\cos\beta_d) + \\
&\quad + b\,(1-k) \\
&= k\frac{a\,(\sin\alpha_d\sin\beta_d - \sin\alpha_d\sin\beta_d) + b\,(\sin\beta_d\cos\alpha_d + \sin\alpha_d\cos\beta_d)}{\cos\beta_d\sin\alpha_d + \cos\alpha_d\sin\beta_d} + b\,(1-k) = b
\end{aligned} \tag{24}$$

Noting that the previous cumulated profile at the grinding point (i.e., $M\,\Delta\theta = 2\pi$, $\boldsymbol{e}_1^{(M)}$) was already equal to "$b$", it is confirmed that a WP profile determined by a one per turn harmonic waviness is not modified by the grinding process. This corresponds, in the affine transformation, to a couple of eigenvalues with unitary modulus and eigenvectors describing a one per turn, complex, harmonic waviness. As this component has no effect on material removal, it has no effect on the final roundness.

On the other side, it can also be demonstrated that, if a profile is not modified by a grinding operation, it implies that there is a 1-per-turn harmonic component, at most null. Let us prove it by construction. Consider a stable profile, with a generic $n$-per-turn not null harmonic component: substituting in Eq.(24), $n$ does not multiplies $\alpha_d$ and $\beta_d$ in the expressions that are used to compute $K_1$ and $K_2$ and therefore the various terms do not cancel out as in the case with $n = 1$. Therefore, after a WP revolution, $\boldsymbol{e}_1^{(N_{WP})} \neq b$, meaning that the material removal has undergone a variation during process execution.

## References


[1] Rowe WB, Richards DL. Geometric Stability Charts for the Centreless Grinding Process. J Mech Eng Sci 1972;14(2):155–60. https://doi.org/10.1243/JMES_JOUR_1972_014_022_02.
[2] Pearce TRA, Stone BJ. Unstable vibration in centreless grinding: Part 1. Geometric instability or chatter? Proc Inst Mech Eng B J Eng Manuf 2011;225(7):1227–43. https://doi.org/10.1177/2041297510393789.
[3] Rowe WB, Barash MM. Computer method for investigating the inherent accuracy of centreless grinding. International Journal of Machine Tool Design and Research 1964;4(2):91–116. https://doi.org/10.1016/0020-7357(64)90002-2.
[4] Rowe WB. Principles of modern grinding technology. 2nd ed. William Andrew Publishing; 2013. ISBN: 978-0-323-24271-4.
[5] Grigoriev SN, Zakharov OV, Li C. Estimation method for geometric stability during shoe-type centerless grinding of rolling bearing parts. Int J Adv Manuf Technol 2024. https://doi.org/10.1007/s00170-024-14034-4.
[6] Hashimoto F, Zhou S. Stability diagram for chatter free centerless grinding and its application in machine development. CIRP Ann Technol 2000;49:225–30.
[7] Hashimoto F, Gallego I, Oliveira JFG, Barrenetxea D, Takahashi M, Sakakibara K, et al. Advances in centerless grinding technology. CIRP Ann 2012;61(2):747–70. https://doi.org/10.1016/j.cirp.2012.05.003.
[8] Inasaki I. Modelling and simulation of grinding processes. CIRP Ann Manuf Technol 1992;41(2):677–88.
[9] Brinksmeier E, Aurich JC, Govekar E, Heinzel C, Hoffmeister HW, Klocke F, et al. Advances in modeling and simulation of grinding processes. CIRP Ann Manuf Technol 2006;55(2):667–96.
[10] Pande SS, Naik AR, Somasundaram S. Computer simulation of the plunge centreless grinding process. J Mater Process Technol 1993;39:179–89.
[11] Li H, Shin YC. A time domain dynamic simulation model for stability prediction of infeed centerless grinding processes. J Manuf Sci Eng 2007;129:539–51.
[12] Garitaonandia I, Fernandes MH, Albizuri J. Dynamic model of a centerless grinding machine based on an updated FE model. Int J Mach Tools Manuf 2008;48:832–40.
[13] Krajnik P, Drazumeric R, Meyer B, Kopac J. Simulation of workpiece forming and centre displacement in plunge centreless grinding. Int J Mach Tools Manuf 2008;48:824–31.
[14] Insperger T, Stépán G, Bayly PV. Regenerative chatter in metal cutting: Analysis and prediction. Annals of the CIRP 2003;52(1):99–102. https://doi.org/10.1016/S0007-8506(07)60544-3.
[15] Zatarain M, Alvarez J, Bediaga I, et al. Implicit subspace iteration as an efficient method to compute milling stability lobe diagrams. Int J Adv Manuf Technol 2015;77:597–607. https://doi.org/10.1007/s00170-014-6470-7.
[16] Leonesio Marco, Bianchi Giacomo. Multistage centerless grinding setup via discrete mapping. J Manuf Process 2022;80:775–88. ISSN 1526-6125,, https://doi.org/10.1016/j.jmapro.2022.06.040.
[17] Insperger T, Stepan G. Semi-discretization for Time-Delay Systems: Stability and Engineering Applications. Springer; 2004.
[18] Hashimoto F. Model Development for Optimum Setup Conditions that Satisfy Three Stability Criteria of Centerless Grinding Systems. Inventions 2017;2(4):26. https://doi.org/10.3390/inventions2040026.
[19] Cui Q, Ding H, Cheng K. An analytical investigation on the workpiece roundness generation and its perfection strategies in centreless grinding. Proc Inst Mech Eng Part B J Eng Manuf 2015;229(3):409–20.
[20] Hashimoto F, Iwashita H. The Effect of Grinding Wheel Contact Stiffness on Plunge Grinding Cycle. Inventions 2020;5(4):62. https://doi.org/10.3390/inventions5040062.
[21] Bianchi G, Leonesio M, Safarzadeh H. A double input describing function approach for stability analysis in centerless grinding under interrupted cut. Int J Adv Manuf Technol 2020;108:439–53. https://doi.org/10.1007/s00170-020-05362-2.
[25] Leonesio M, Parenti P, Bianchi G. Frequency domain identification of grinding stiffness and damping. Mech Syst Signal Process 2017;93:545–58. https://doi.org/10.1016/j.ymssp.2017.02.028.
[26] Leonesio M. Physics-enhanced machine learning methods for industrial process modeling and optimization, Ph.D. dissertation. Politecnico di Milano; 2025.
[27] Xie Peichen. Hyb error: a hybrid metric combining absolute and relative errors. 2024. arXiv:2403.07492v2 [math.NA].

[28] Strang G. Linear Algebra and Its Applications. 4th ed. Cengage Learning; 2006.
[30] Hoerl AE, Kennard RW. Ridge regression: Biased estimation for nonorthogonal problems. Technometrics 1970;12(1):55–67.
[32] Davis Philip J. Circulant Matrices. New York: Wiley; 1970. ISBN 0–471–05771-1.
[33] Mitutoyo. Round Test 2200H, datasheet: *2009_RA-2200.pdf*. 2009.
[34] Zhang Jing, He Chunlei, Chen Guang, Luo Meijun, Ren Chengzu. Roundness variation of tapered rollers in double-disc straight groove lapping process. J Manuf Process 2024;126:413–28. ISSN 1526-6125,, https://doi.org/10.1016/j.jmapro.2024.07.116.